

**THE CAUSES OF PROPELLER PITCHING MOMENT AND THE CONDITIONS
FOR ITS SIGNIFICANCE**

A Dissertation
Presented to
The Academic Faculty

By

Xiaofan Fei

In Partial Fulfillment
of the Requirements for the Degree
Doctor of Philosophy in the
School of Aerospace Engineering

Georgia Institute of Technology

December 2021

THE CAUSES OF PROPELLER PITCHING MOMENT AND THE CONDITIONS FOR ITS SIGNIFICANCE

Thesis committee:

Dr. Brian J. German
School of Aerospace Engineering
Georgia Institute of Technology

Dr. Marilyn J. Smith
School of Aerospace Engineering
Georgia Institute of Technology

Dr. Dimitri N. Mavris
School of Aerospace Engineering
Georgia Institute of Technology

Dr. Nicholas K. Borer
Aeronautics Systems Analysis Branch
NASA Langley Research Center

Dr. Lakshmi N. Sankar
School of Aerospace Engineering
Georgia Institute of Technology

Date approved: April 23, 2021

Wise men learn from fools. Fools learn from no man.

?

To my wife, Yuqian.

ACKNOWLEDGMENTS

They say that a PhD is a journey of self-discovery. From the beginning, my parents have pushed me to achieve while allowing me the freedom to pursue my passions. They instilled in me a sense of standard and pride in one's work, regardless of application. In college, I was accepted by an advisor who would teach me how to learn. His patient guidance through a wide array of academic interests instructed me on the philosophy of higher education and the importance of finding my motivations. My fellow labmates at the German Research Group also taught me many of the foundational skills that I rely upon today. The past few years, I have had the honor of interning in the Aeronautics Systems Analysis Branch at NASA Langley. My mentors here show me that the impact of one's work should be greater than on oneself. Through all of this, my dear wife has supported me with immeasurable tolerance. Her dedication and kindness is a brilliant reminder of one's responsibility to others that continuously drives me to be a better person. Finally, I turn my thoughts forward to my committee members, who have graciously donated their time toward validating my efforts and are sure to challenge me in the defense ahead.

As much a journey of self-discovery, my PhD has been a discovery of family and friends. To all of you who have helped me academically, professionally, financially, and emotionally over the years, *thank you*.

This work was funded under the Transformational Tools and Technologies Project of the Transformative Aeronautics Concepts Program. A special thanks to David J. Pate, who provided the GPU-computing function for RoBIN's Biot-Savart calculations, and to Brandon L. Litherland, who provided the OVERFLOW CFD results for comparison.

TABLE OF CONTENTS

Acknowledgments	v
List of Figures	ix
Summary	xiii
Chapter 1: Introduction	1
1.1 Background	1
1.2 Organization of Work	3
1.3 Limitations and Definitions	4
Chapter 2: Hypotheses for the Causes of Propeller Pitching Moment	6
2.1 Advancing-Retreating Blade Effect	7
2.2 Skewed-Wake Effect	8
2.3 Influence of a Wing	12
2.4 Summary of Hypotheses	13
Chapter 3: Development of an Unsteady Vortex Lattice Method for Modeling Propellers at Angle of Attack	14
3.1 Method Overview	15
3.2 Influence Matrices	16

3.3	Inset Distance	17
3.4	Vortex Core Model	17
3.5	Slow-start Rev-up	18
3.6	Load Calculation	19
Chapter 4: Model Evaluation		22
4.1	Geometry	22
4.2	Simulation Time Convergence	23
4.3	Grid Resolution and Time Step Resolution Convergence	25
4.4	Accuracy Compared to CFD	27
4.4.1	OVERFLOW Setup	28
4.4.2	Angle of Attack Sweep for Isolated Propeller	29
4.4.3	Force Distribution Comparisons	31
4.4.4	Angle of Attack Sweep for Propeller and Wing	33
4.5	Computation Time	38
Chapter 5: Investigating the Causes of Propeller Pitching Moment		39
5.1	Geometry	39
5.2	Testing the Effect of a Skewed Propeller Wake	41
5.3	Testing the Effect of Wing Circulation	44
Chapter 6: Investigating the Conditions for Significance		48
6.1	Pitching Moment Trends during Transition	48
6.2	A Generalizable Metric for Significance	52

6.3	The Effect of Design Parameters on the Significance of Propeller Pitching Moment	55
Chapter 7: Conclusion and Recommendations		61
7.1	Impacts on Aircraft Design	61
7.2	Recommendations for Future Work	63
Appendices		64
Appendix A: Constancy of Aerodynamic Coefficients with Advance Ratio		65
Appendix B: Propeller in Forward Flight Validation		67
References		70

LIST OF FIGURES

1.1	Propeller reference frame and component forces and moments generated by a propeller at an angle of attack. Arrows denote positive convention. . .	5
2.1	Decomposition of the total velocity at a blade section. Adapted from [14]. .	7
2.2	Comparison of velocity components and sectional forces on a blade section at $\phi = 90^\circ$ and $\phi = 270^\circ$	8
2.3	Comparison of the axial induced velocity components on a propeller at zero and nonzero angle of attack.	10
2.4	Asymmetric influence of a skewed wake on the axial induced velocity at the propeller disk.	10
2.5	Comparison of velocity components and sectional forces on a blade section at $\phi = 0^\circ$ and $\phi = 180^\circ$	12
2.6	Asymmetric influence of a wing positioned behind the propeller on the induced velocity at the propeller disk.	13
3.1	Generation of bound geometry in RoBIN.	16
4.1	HLP blade geometry.	23
4.2	X-57 HLP and wing as modeled in RoBIN visualized with a notional prescribed wake.	23
4.3	RoBIN convergence behavior with respect to number of revolutions. . . .	24
4.4	Demonstration of increasingly strong wake distortions with propeller angle of attack.	25
4.5	RoBIN convergence behavior with respect to grid resolution. $\alpha_p = 30^\circ$. . .	26

4.6	RoBIN convergence behavior with respect to time step resolution. $\alpha_p = 30^\circ$.	27
4.7	Comparison of RoBIN and OVERFLOW results for the isolated HLP over a sweep of α_p .	30
4.8	Comparison of inviscid (RoBIN) and viscous (XFOIL) lift curves for the MH 114 airfoil.	30
4.9	Contours of $-F'_x$ and $-F'^*_x$ at $\alpha_p = 30^\circ$ overlaid on a colored map of the dimensional error. Solid contours are from RoBIN and dashed contours are from OVERFLOW.	32
4.10	Contours of $-F'_x$ and $-F'^*_x$ at $\alpha_p = 30^\circ$ overlaid on a colored map of the normalized error. Solid contours are from RoBIN and dashed contours are from OVERFLOW.	33
4.11	Shaded map of the component of kinematic velocity in the spanwise direction over a blade at various azimuthal positions. Positive values defined as inward toward the center.	34
4.12	Contours of F'_y and F'^*_y at $\alpha_p = 30^\circ$ overlaid on a colored map of the dimensional error. Solid contours are from RoBIN and dashed contours are from OVERFLOW.	35
4.13	Contours of F'_z and F'^*_z at $\alpha_p = 30^\circ$ overlaid on a colored map of the dimensional error. Solid contours are from RoBIN and dashed contours are from OVERFLOW.	36
4.14	Comparison of RoBIN and OVERFLOW results for the propeller in the propeller and wing case over a sweep of α_p with isolated propeller results included.	37
4.15	Comparison of RoBIN and OVERFLOW results for the wing in the propeller and wing case over a sweep of α_p .	37
5.1	Generic propeller and wing as modeled in RoBIN visualized with a notional prescribed wake.	41
5.2	Comparison of propeller forces and moments over a sweep of α_p using prescribed wake and free wake modes.	42
5.3	Contours of total axial induced velocity observed by the blades over the last revolution at $\alpha_p = 30^\circ$. Prescribed wake mode (left) and free wake mode (right).	43

5.4	Contours of bound vortex rings' contribution to axial induced velocity observed by the blades at $\alpha_p = 30^\circ$. Prescribed wake mode (left) and free wake mode (right).	43
5.5	Contours of wake vortex rings' contribution to axial induced velocity observed by the blades at $\alpha_p = 30^\circ$. Prescribed wake mode (left) and free wake mode (right).	44
5.6	Comparison of propeller forces and moments over a sweep of α_p with varying α_w .	45
5.7	Contours of total axial induced velocity observed by the blades over the last revolution at $\alpha_p = 0^\circ$. $i_w = 0^\circ$ (left) and $i_w = 20^\circ$ (right).	46
5.8	Contours of the propeller's bound and wake vortex rings' contribution to axial induced velocity observed by the blades at $\alpha_p = 0^\circ$. $i_w = 0^\circ$ (left) and $i_w = 20^\circ$ (right).	46
5.9	Contours of the wing's bound and wake vortex rings' contribution to axial induced velocity observed by the blades at $\alpha_p = 0^\circ$. $i_w = 0^\circ$ (left) and $i_w = 20^\circ$ (right).	47
6.1	Surface of $C_{My}/-C_{Fx}$ over advance ratio and angle of attack.	50
6.2	Wake visualization at a selection of advance ratios. $\alpha_p = 90^\circ$, $N_{rev} = 8$, freestream direction left to right.	51
6.3	Surface of C_{My}^∞ over advance ratio and angle of attack.	52
6.4	Surface of $-C_{Fx}^\infty$ over advance ratio and angle of attack.	53
6.5	Example surface of $N_p M_y/Wc$ over freestream velocity and angle of attack.	55
6.6	Surface of $N_p M_y/Wc$ with $N_p = 3$.	56
6.7	Surface of $N_p M_y/Wc$ with $N_p = 12$.	56
6.8	Surface of $N_p M_y/Wc$ with $p_{DL} = 2.5 \text{ lb/ft}^2$.	58
6.9	Surface of $N_p M_y/Wc$ with $p_{DL} = 10 \text{ lb/ft}^2$.	58
6.10	Surface of $N_p M_y/Wc$ with $C_L = 0.325$.	59
6.11	Surface of $N_p M_y/Wc$ with $C_L = 1.3$.	59

6.12	Surface of $N_p M_y / W c$ with $p_{WL} = 7.5 \text{ lb/ft}^2$	60
6.13	Surface of $N_p M_y / W c$ with $p_{WL} = 30 \text{ lb/ft}^2$	60
A.1	Thrust coefficients versus advance ratio for generic propeller at $\alpha_p = 60^\circ$. .	66
A.2	Pitching moment coefficients versus advance ratio for generic propeller at $\alpha_p = 60^\circ$	66
B.1	Thrust coefficient vs advance ratio for isolated HLP.	68
B.2	Power coefficient vs advance ratio for isolated HLP.	69

SUMMARY

Recent development of vertical takeoff and landing (VTOL) aircraft has renewed interest in the study of propellers. One metric in particular, the propeller pitching moment, has been observed to be important to VTOL aircraft stability and control in the past. Propellers at angles of attack could not be accurately modeled in generations past due to a lack of computational power, but even with advances in computer technology, modern designers seem to possess insufficient knowledge in this area. In this dissertation, we study the physics behind propeller pitching moment in the context of an isolated propeller and a propeller upstream of a wing. An unsteady 3D vortex lattice method is developed specifically to model propellers at angles of attack and is validated by comparing to high-fidelity CFD analyses. We then use the model to isolate velocity influences to show that the propeller pitching moment is largely caused by two effects: a skewed wake and the presence of wing circulation. Generated maps of propeller pitching moment over a range of operational parameters corresponding to VTOL transition show that the low flight speeds and high angles of attack encountered during transition lead to significant magnitudes of propeller pitching moment that would be difficult to trim using passive methods. Also, derivation of a generalizable metric of significance shows that the peak contribution of propeller pitching moment to aircraft stability is comparable to a longitudinal displacement of the center of gravity by several percent of the wing chord. Finally, we give a concluding discussion on the impact of propeller pitching moment on VTOL aircraft design.

CHAPTER 1

INTRODUCTION

In the conceptual design of conventional propeller aircraft, thrust and torque are the primary propeller metrics of concern to the designer. Secondary effects such as the longitudinal in-plane normal force or the lateral out-of-plane yawing moment (sometimes referred to as the p-factor) may be considered if the aircraft is expected to operate beyond low angles of attack during maneuvers or during takeoff and landing, but these effects rarely constrain the aircraft design.

The recently renewed interest in vertical takeoff and landing (VTOL) aircraft has led to aircraft concepts such as tiltwings and tiltrotors that require operating propellers at much higher angles of attack during the transition from hover to forward flight. Propellers operated in this way will produce non-negligible secondary forces and moments that may compromise aircraft stability and controllability if not accounted for early in the design process. One effect in particular, the propeller pitching moment, has received little attention due to its insignificance to conventional aircraft, but we suspect that it will be important for propeller-driven VTOL aircraft based on past experimental observations.

This dissertation studies the propeller pitching moment in the context of both isolated propellers and wing-mounted propellers operating at nonzero angles of attack. A computational model is developed to investigate the underlying physics and to explore the conditions under which propeller pitching moment would be most significant to aircraft.

1.1 Background

In the mid-to-late 1900s, the US government and aviation industry made a concerted effort to research and develop VTOL fixed-wing aircraft. Although this effort was largely unsuccessful in realizing production VTOL aircraft, the extensive ground and flight testing

performed across multiple design programs led to valuable insights into the challenges of VTOL aircraft—chief among them, stability and control during hover and transition [1]. Of particular interest was a nose-up pitching moment during transition that was observed in concepts that required tilting the propeller, such as the Curtiss-Wright X-100 tiltprop [1] and the Vertol VZ-2 tiltwing [2–6]. Some deflected slipstream concepts, such as the Fairchild VZ-5 [7], also experienced pitching moment problems while others, such as the Ryan VZ-3RY [8–10], did not. Supplemental wind tunnel tests attributed the pitching moment to the propeller, which was observed to generate a pitching moment when operated at an angle to the freestream [11]. Furthermore, the pitching moment was magnified when the propeller was positioned in front of a wing [12]. The presence of this pitching moment was a hurdle for VTOL aircraft designers because established propeller models of the time were unable to predict this effect with adequate accuracy.

The aeronautics literature concerning propeller secondary effects has been (and still is) concentrated on the study of normal force and yawing moment. Works dating to as early as 1909, according to reviews by Ribner [13] and Phillips et al. [14], indicate an understanding of the advancing-retreating blade effect's role in the generation of normal force and yawing moment. One of the earliest analytical models that appropriately accounted for induced velocity was presented by Ribner [13] for propellers at small angles of yaw. De Young [15] then expanded Ribner's work to propellers at higher angles. Modern authors have continued to improve on analytical models of normal force and yawing moment [14], but the understanding of the underlying physics has remained unchanged.

In contrast, no satisfactory explanations of propeller pitching moment have been found despite multiple experiments having documented its existence [16–21]. Early attempts to reconcile the presence of pitching moment in experimental results with the lack thereof in theoretical models led to the development of a phase lag angle model [15, 22, 23] that analogized the propeller blades to a harmonically oscillating wing. However, the phase lag angle method was shown to perform poorly when validated against experimental results

[24]. Another analytical model, by Lehman, was referenced for the propeller design of the Curtiss-Wright X-19 [25] but was also described as being inaccurate when compared to experimental data. The X-19 designers did suspect, however, that propeller secondary effects were likely strongly dependent on the induced velocity field but concluded that modeling the induced velocity field of an inclined propeller was beyond their capabilities at the time.

Perhaps an artifact of past limitations, modern propeller studies utilizing higher-order induced velocity models [26], unsteady vortex lattice methods [27], or Navier-Stokes CFD methods [28] that should be capable of analyzing propeller pitching moment still tend to omit it from discussion. Some recognition can be found in the horizontal-axis wind turbine literature [29] under the guise of lateral stability in yawed conditions, or in the quadrotor literature [30, 31], where the rotors in edgewise flight are essentially propellers at high angle of attack. Description of similar effects in rotorcraft literature also exist. For example, helicopters experience a phenomenon known as “blowback” in which a nose-up pitching moment occurs upon initiating forward motion from hover [32]. However, discussions based on rotorcraft aerodynamics should be interpreted with caution because the behavior of rotors with flexible, hinged blades and cyclic pitch control may not be representative of the behavior of rigid fixed-pitch propellers.

1.2 Organization of Work

The goal of this dissertation is to answer the following two research questions:

RQ1: What are the causes of propeller pitching moment?

RQ2: Under what conditions does propeller pitching moment become significant for aircraft flight dynamics?

The subsequent chapters are organized as follows: Chapter 2 first posits hypotheses for RQ1 based on a first-principles analysis of the problem. Chapter 3 then details the development of an unsteady vortex lattice method tailored for modeling propellers at nonzero

angles of attack, and Chapter 4 validates said model in terms of convergence characteristics and accuracy. In Chapter 5, the developed model is used to test the hypotheses from Chapter 2 and to answer RQ1, and in Chapter 6, the model is used to explore a range of operating conditions corresponding to VTOL transition to answer RQ2. Lastly, Chapter 7 concludes with a discussion on the implications of the presented results on VTOL aircraft design.

1.3 Limitations and Definitions

The secondary propeller effects of interest to this dissertation are the resulting time-average of the blades' cyclic instantaneous loads, sometimes referred to as 1P or Aq loads¹. The unsteady loading of individual blades is important to propeller acoustics and fatigue analysis [33, 34] but is not considered here. Additionally, the analysis herein assumes propellers to be rigid and to rotate clockwise when viewed from the aft looking forward. Figure 1.1 defines the propeller reference frame and conventions used. Here, $-F_x$ is thrust and M_x is shaft torque. The secondary effects include F_y as the side force, F_z as the normal force, M_y as the pitching moment, and M_z as the yawing moment.

Some of the studies presented herein will involve the interaction of a propeller a wing. An important distinction to be made is that, in these cases, our focus is on the performance of the propeller and not on that of the wing. There exists a plethora of literature on propeller-wing interaction [35–77], but the vast majority only consider the change in the performance of the wing. Those that include analysis on the propeller also typically only consider thrust and power.

¹1P refers to their once-per-revolution frequency, and Aq derives from the proportionality of these loads to the product of the inflow angle, A , and dynamic pressure, q , for small inflow angles.

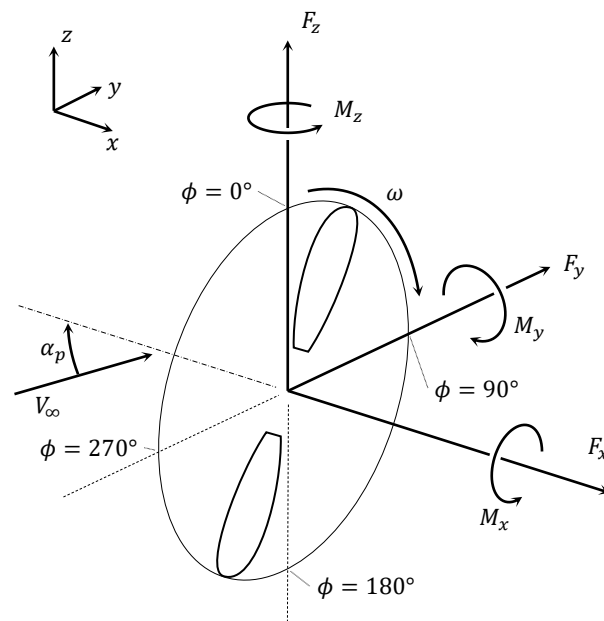


Figure 1.1: Propeller reference frame and component forces and moments generated by a propeller at an angle of attack. Arrows denote positive convention.

CHAPTER 2

HYPOTHESES FOR THE CAUSES OF PROPELLER PITCHING MOMENT

The total velocity, V_{tot} , observed by a blade section of an isolated propeller can be expressed as a vector sum of components from three sources: the freestream velocity from forward motion, V_∞ ; the tangential velocity from propeller rotation, $\omega \times r$; and the induced velocity from the blades and their wakes, V_i . When the propeller is at an angle of attack, α_p , defined about the y axis as illustrated in Figure 1.1, the contribution of V_∞ is not constant and varies with blade azimuthal position, ϕ . Consider the velocity diagram shown in Figure 2.1 for a generic blade section located at radius r and azimuth ϕ on a propeller at angle α_p to the freestream. The decomposition of V_∞ is given by

$$V_{\infty,x} = V_\infty \cos \alpha_p \quad (2.1)$$

$$V_{\infty,\phi} = V_\infty \sin \alpha_p \sin \phi \quad (2.2)$$

The presence of $\sin \phi$ in the magnitude of the tangential freestream velocity component, $V_{\infty,\phi}$, indicates that V_{tot} will vary with azimuthal position, resulting in unsteady cyclic loads as the blade revolves. However, if $V_{\infty,\phi}$ were the only component to vary azimuthally, then there would be zero pitching moment because the distribution of $V_{\infty,\phi}$ is symmetric about the y axis (e.g., $V_{\infty,\phi}$ at $\phi = 45^\circ$ is identical to $V_{\infty,\phi}$ at $\phi = 135^\circ$). Thus, for pitching moment to be nonzero, there must exist an asymmetric distribution of V_i about the y axis over the propeller disk. In the subsequent sections, we will derive hypotheses for the causes of propeller pitching moment by examining three potential sources of induced velocity asymmetry.

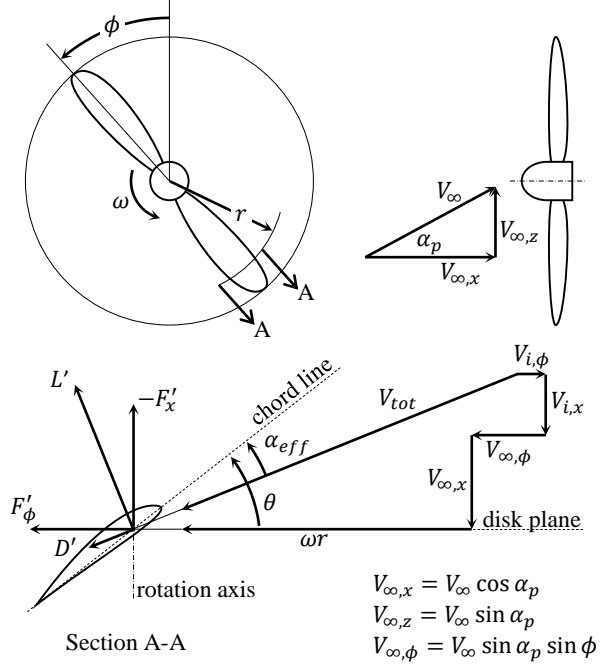


Figure 2.1: Decomposition of the total velocity at a blade section. Adapted from [14].

2.1 Advancing-Retreating Blade Effect

One of the most well-understood sources of flow asymmetry on a propeller is the advancing-retreating blade effect. Consider the velocities and sectional forces experienced by a blade section at the $\phi = 90^\circ$ and $\phi = 270^\circ$ positions on a propeller at $\alpha_p > 0^\circ$, as depicted in Figure 2.2. At $\phi = 90^\circ$, the blade is rotating partly against the freestream direction (i.e., advancing) such that the component of freestream velocity in the tangential direction, $V_{\infty,\phi}$, adds to the rotational velocity, ωr . In contrast, at $\phi = 270^\circ$, the blade is rotating partly along the freestream direction (i.e., retreating) such that $V_{\infty,\phi}$ subtracts from ωr . The asymmetry in $V_{\infty,\phi}$ results in the $\phi = 90^\circ$ position experiencing a larger α_{eff} and V_{tot} than the $\phi = 270^\circ$ position, both of which serve to increase the L' and D' produced at $\phi = 90^\circ$, assuming stall does not occur¹. Projecting the sectional forces in the axial and tangential directions then shows that a positive yawing moment would be generated about the propeller origin from the difference in $-F'_x$ and that a positive normal force would be

¹Although it is possible for D' to decrease with increasing α_{eff} if α_{eff} is below the blade section airfoil's minimum drag angle of attack, the blades on most practical propellers would not operate in this regime.

generated from the difference in F'_ϕ . In actuality, the physics are complicated by an additional asymmetry—the higher lift generated by the advancing blade results in stronger vorticity being shed and, therefore, larger induced velocity components at $\phi = 90^\circ$ than at $\phi = 270^\circ$. This asymmetry in induced velocity partially counteracts the effect of $V_{\infty,\phi}$ on α_{eff} and is expected to be important for the accurate modeling of normal force and yawing moment; omission of the asymmetric induced velocity would likely result in overpredictions of both. However, because the induced velocity is a reaction to the lift which, in turn, depends on $V_{\infty,\phi}$, any variation in induced velocity due to the advancing-retreating blade effect should still nominally be symmetric about the y axis and should not be a cause of propeller pitching moment.

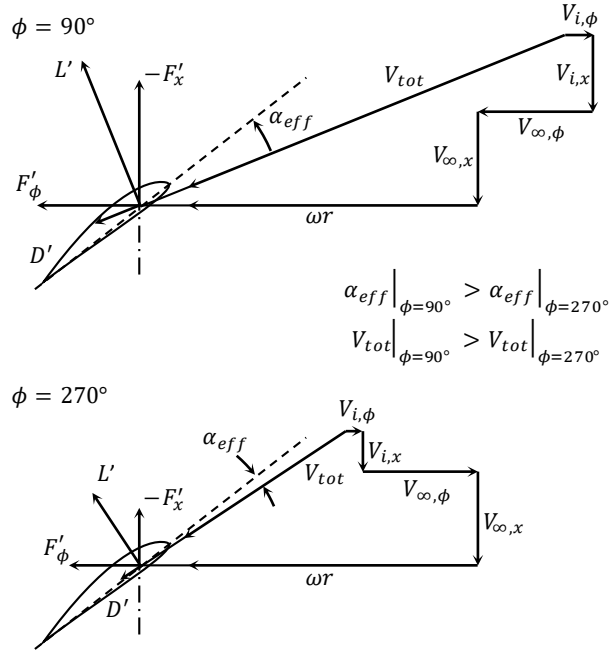


Figure 2.2: Comparison of velocity components and sectional forces on a blade section at $\phi = 90^\circ$ and $\phi = 270^\circ$.

2.2 Skewed-Wake Effect

Another possible source of induced velocity asymmetry is the skewing of the wake when a propeller is at a nonzero angle of attack. For the isolated propeller, consider the cases

when $\alpha_p = 0^\circ$ and $\alpha_p > 0^\circ$, as illustrated in Figure 2.3. When $\alpha_p = 0^\circ$, the wake structure is axisymmetric about the rotation axis and the tip vortices induce an axial component of velocity, $V_{i,x}$, in the $+x$ direction at the propeller disk. When $\alpha_p > 0^\circ$, the wake becomes skewed in the direction of the freestream and the induced velocity distribution at the propeller disk would no longer be symmetric about the y axis. The vorticity shed from the downwind side (blue arrows) continues to induce a velocity component in the $+x$ direction at the propeller disk but is now in closer proximity to the downwind side than the upwind side. Meanwhile, the vorticity shed from the upwind side (red arrows) is now positioned to induce a $V_{i,x}$ component in the $-x$ direction on portions of the upwind side of the propeller disk. Consequently, the downwind side of the propeller disk will experience an overall larger (i.e., more positive) induced velocity component in the axial direction than the upwind side. Figure 2.4 demonstrates the aforementioned asymmetry as effected by a pair of differential vortex segments, $d\mathbf{l}$, that were shed from the $\phi = 0^\circ$ and $\phi = 180^\circ$ positions one revolution ago. In the top diagram of Figure 2.4, the $\phi = 180^\circ$ vortex segment points into the page, and its influence at two equiradial points on the propeller disk, P^U and P^D , results in $d\mathbf{V}_{i,x}^U$ and $d\mathbf{V}_{i,x}^D$ of opposing directions. In the bottom diagram, the $\phi = 0^\circ$ vortex segment points out of the page, and its influence at the same two equiradial points results in $d\mathbf{V}_{i,x}^U$ and $d\mathbf{V}_{i,x}^D$ in the same $+x$ direction. However, $d\mathbf{V}_{i,x}^D$ is of larger magnitude than $d\mathbf{V}_{i,x}^U$ due to the inverse-square relationship of the Biot-Savart law with distance, s :

$$d\mathbf{V}_i = \frac{\Gamma}{4\pi} \frac{d\mathbf{l} \times \mathbf{s}}{s^3} \quad (2.3)$$

where Γ is the strength of vortex segment $d\mathbf{l}$ and \mathbf{s} is the distance vector from $d\mathbf{l}$ to P . Integrating $d\mathbf{V}_{i,x}$ over all $d\mathbf{l}$ gives the aggregate effect illustrated in Figure 2.3. Note that the tangential component of induced velocity, $V_{i,\phi}$, which is dependent on the wake helix angle, is assumed to be relatively invariant between the upwind and downwind sides of the propeller.

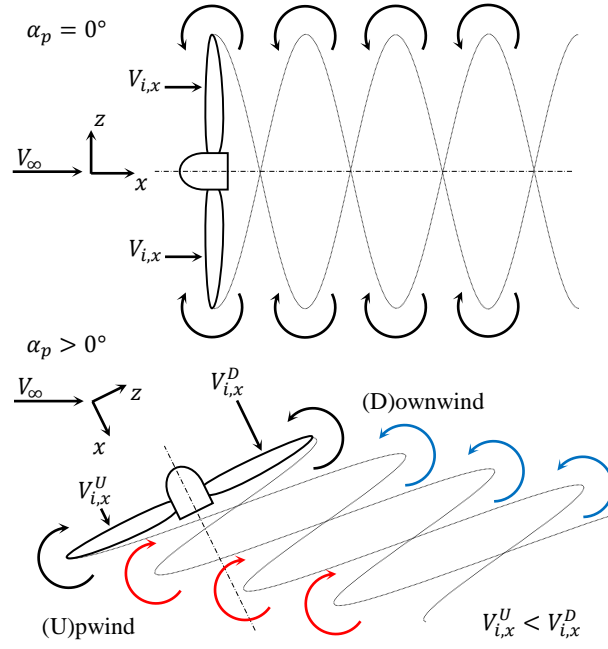


Figure 2.3: Comparison of the axial induced velocity components on a propeller at zero and nonzero angle of attack.

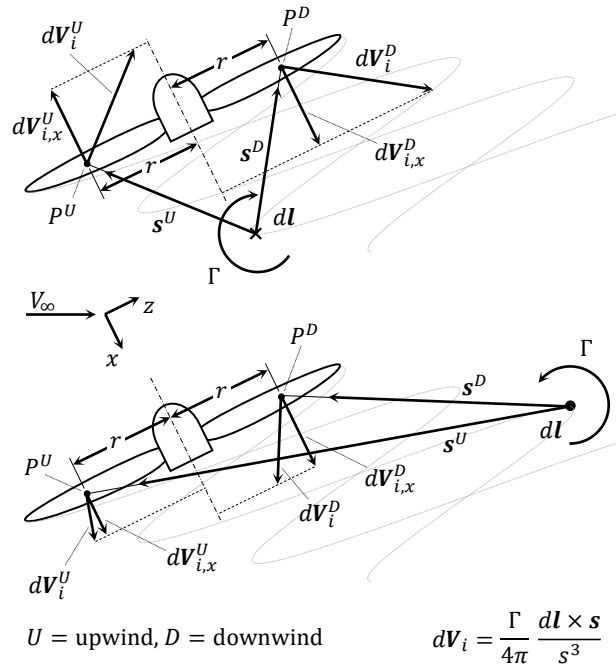


Figure 2.4: Asymmetric influence of a skewed wake on the axial induced velocity at the propeller disk.

The effect of the asymmetric distribution of $V_{i,x}$ is shown in Figure 2.5, which depicts the velocities and sectional forces experienced by blade sections at the $\phi = 0^\circ$ and $\phi = 180^\circ$ positions on a propeller at $\alpha_p > 0^\circ$. At these azimuthal positions, $V_{\infty,\phi}$ vanishes so the only difference is due to the variation in induced velocity. A variation in $V_{i,x}$ produces competing effects on sectional forces; increasing $V_{i,x}$ increases the magnitude of V_{tot} but decreases the effective angle of attack, α_{eff} . In practice, the effect of α_{eff} on sectional forces is more dominant than that of $V_{i,x}$, and thus, the blade at $\phi = 0^\circ$ produces a lower sectional lift, L' , and sectional drag, D' , than the blade at $\phi = 180^\circ$. Projection of the sectional forces in the axial direction, $-F'_x$, reveals a thrust asymmetry that would result in a positive pitching moment about the propeller origin.

Technically, a side force is also generated from the asymmetry in the sectional tangential forces, F'_ϕ , but the magnitude would be very small when compared to the propeller thrust. F'_ϕ (which is not drawn to scale in Figure 2.5) is usually at least an order of magnitude smaller than $-F'_x$, and the difference between F'_ϕ at different azimuthal positions would be even less.

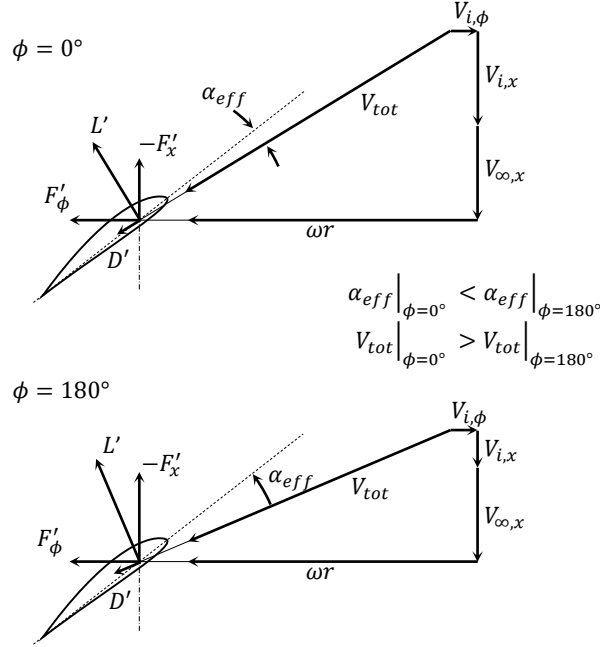


Figure 2.5: Comparison of velocity components and sectional forces on a blade section at $\phi = 0^\circ$ and $\phi = 180^\circ$.

2.3 Influence of a Wing

Lastly, velocity asymmetries could also be induced by external sources such as a nearby wing. The influence of a wing behind the propeller can be inferred in a similar manner to that of the propeller wake. Figure 2.6 shows the asymmetric influence of a wing's circulation on a propeller at $\alpha_p = 0^\circ$, where the wing is represented by a lifting line segment, $d\mathbf{l}$, of strength Γ pointing into the page. The induced velocities at two equiradial points on the propeller are shown with decompositions in the x and z directions. Similar to the top diagram in Figure 2.4, the circulation about the wing results in a $\mathbf{V}_{i,x}$ in the $-x$ direction on the upwind side of the propeller and a $\mathbf{V}_{i,x}$ in the $+x$ direction on the downwind side. The effect of the asymmetric $\mathbf{V}_{i,x}$ on sectional forces would be similar to that described in Figure 2.5, resulting in a positive pitching moment. The circulation also induces a positive $\mathbf{V}_{i,z}$ over the propeller disk so the effects associated with the advancing-retreating blade effect described in Section 2.1 may be produced to some degree. If wing thickness is

modeled, then an additional blockage effect would reduce $V_{i,x}$ in the immediate upstream vicinity. A propeller positioned with its hub above the wing would experience a further increase in positive pitching moment whereas a propeller mounted below the wing would see a decrease in pitching moment.

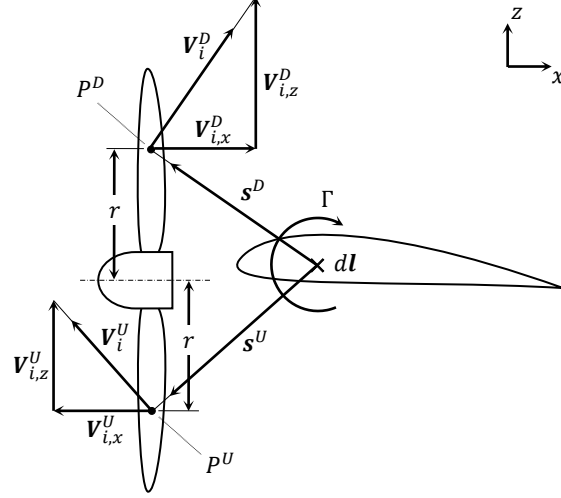


Figure 2.6: Asymmetric influence of a wing positioned behind the propeller on the induced velocity at the propeller disk.

2.4 Summary of Hypotheses

Based on the previous theoretical analyses, we hypothesize that:

- 1) The pitching moment of an isolated propeller at an angle of attack is caused by the skewed wake generating an asymmetric axial induced velocity distribution over the propeller disk.
- 2) The pitching moment produced by a propeller when positioned in front of a wing is caused by an asymmetric axial induced velocity distribution generated by the wing's circulation over the propeller disk.

CHAPTER 3

DEVELOPMENT OF AN UNSTEADY VORTEX LATTICE METHOD FOR MODELING PROPELLERS AT ANGLE OF ATTACK

To test our hypotheses, we would like a simple tool that can accurately model propellers at angles of attack without being prohibitively expensive (both monetarily and computationally), but such a tool could not be found at the time of this research. Grid-based CFD codes were considered too time consuming for exploratory studies, and blade-element-with-inflow models had been shown to be unreliable for propellers at high angles of attack [78]. Therefore, we developed a new vortex lattice method (VLM) based on established formulations found in the literature. A VLM was a suitable approach because it would innately capture the interactions between the propeller and its wake, and the vortex elements' induced velocity influences could be attributed to distinct contributing sources.

Historically, VLMs have seen extensive use in the modeling of propellers, including conventional air propellers [79, 80], ducted fans [81], contra-rotating propellers [82], and marine propellers [83, 84]. These implementations have typically used prescribed helical vortex filament wake structures and are suitable for steady, axial flight operating conditions. However, vortex filament wake structures cannot accurately model the wakes of propellers at angle of attack. The unsteady blade loading causes vorticity to be shed in both the streamwise and radial directions, and vortex filaments would only be able to capture the streamwise component. More recently, improvements in computing speed have led to an increase in the popularity of free vortex ring wake formulations. Vortex ring elements can capture the radial vorticity [27, 85], and the free wake formulation allows for better wake fidelity under high loading conditions [86].

This chapter presents the development of a 3D unsteady VLM with free wake propagation, dubbed RoBIN (Rotating Blades at Incidence in Nonuniform flow), based on Katz

and Plotkin’s vortex ring formulation (found in Section 13.12 of reference [87]). Since [87] already provides a detailed discussion of the underlying theory, this chapter will focus on additions to and deviations from the original formulation. The discussion is given in the context of rotating propeller blades, but the formulation is easily extended to wings by omitting the rotational aspect.

3.1 Method Overview

A blade is represented in RoBIN as a structured grid of constant strength quadrilateral vortex rings bound to the mean camber surface. To generate this bound vortex geometry, the physical (mean camber surface) geometry is first discretized into a structured grid with user-specified numbers of panels in the chordwise and spanwise directions. The leading segment of a vortex ring is then placed on each panel’s quarter chord line, and the trailing segment is placed at the quarter chord line of the next chordwise panel. For panels at the blade’s trailing edge, the trailing segment is placed somewhere in the flow behind the panel as a lump sum representation of the radially oriented vorticity shed over the last time step (or of the starting vortex in the case of $t = 0$). Katz and Plotkin suggest a location on the path of the trailing edge over the last time step at a distance 0.2-0.3 times the length of said path away from the trailing edge, and an average value of 0.25 was selected for RoBIN. The side segments connect the leading and trailing segments to form a closed ring. Figure 3.1 illustrates the geometry generation process as described thus far.

The vortex ring strengths are solved with a system of equations that satisfies the Neumann boundary condition at a collocation point for each ring. This collocation point is located chordwise at the $3/4$ -chord location on the respective panel and spanwise at the mid-point for uniformly spaced panels. James [88] showed this $1/4$ -chord, $3/4$ -chord placement of the leading segment and collocation point, known as the Pistoletti approximation [89], to be highly accurate for its level of simplicity, and although more sophisticated placement schemes exist [90], they were not employed for the current effort.

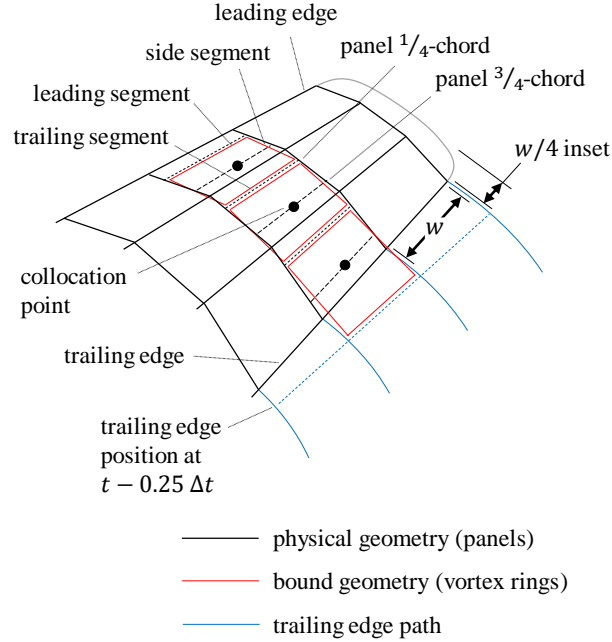


Figure 3.1: Generation of bound geometry in RoBIN.

At each time step, the geometry is first progressed by a prescribed motion, and the wake vortex rings' corner points are propagated (via the first order explicit Euler method) by the local velocities calculated at the end of the previous time step. Then, a new row of wake vortex rings is shed with strengths equal to those of the bound trailing edge rings', filling the newly formed gap between the bound and wake vortex sheets. Finally, the bound vortex ring strengths are updated, and the local velocities at the wake corner points are calculated for the next time step.

3.2 Influence Matrices

An important implication of Katz and Plotkin's suggested method for placing trailing edge trailing segments is that the bound geometry will change with blade azimuthal position when propeller angle of attack is nonzero. Specifically, the vortex rings along the trailing edge will be stretched in the streamwise direction when the blade is advancing and will be shortened when the blade is retreating because of the freestream velocity's azimuthally varying contribution to the trailing edge's path. Consequently, a unique influence matrix

will be required for each unique orientation of the propeller. To limit the number of unique orientations and allow for the pre-calculation of all influence matrices, RoBIN requires a time step size such that a revolution will be completed in a whole number of time steps. Pre-calculating the influence matrices trades off computation time for memory storage, but influence matrix size has not posed a problem for the grid resolutions investigated here.

3.3 Inset Distance

In generating the bound geometry, an inset distance, illustrated in Figure 3.1, is applied at the blade tip to help increase the convergence rate of the solution with respect to grid resolution. While the optimal inset distance depends on the load distribution over the blade [91], $w/4$ has been shown to be a good approximation for open-tipped lifting surfaces [81], where w is the spanwise width of a uniformly discretized panel. For the blade-only geometry used in Chapter 4, the inset distance was applied at both the tip and root since a spinner was not present.

3.4 Vortex Core Model

A common issue with free wake methods is that wake vortex segments can come in close proximity with each other due to wake roll up. Left alone, the nonlinearly increasing velocity influence with decreasing distance from a vortex singularity can lead to wake points experiencing unreasonably large changes in position over a single time step. RoBIN addresses this issue with a vortex core model to smooth the velocity influence in the close vicinity of a vortex segment. The model, presented by Ramasamy [92], combines a vorticity strain model by Anarath et al. [93] with the vorticity diffusion model by Bhagwat and Leishman [94]. After some rearrangement, Ramasamy's model gives the vortex core radius as

$$r_{vc}(t) = \sqrt{r_0^2 + 4\alpha_o t(\nu + a_1\Gamma) \left(\frac{l_0}{l}\right)} \quad (3.1)$$

where $r_{vc}(t)$ is the core radius at time t , r_0 is the initial core radius, α_o is the Oseen constant with a value of 1.25643, ν is the kinematic viscosity, a_1 is Squire's coefficient with an estimated value of 2e-4 based on empirical data [92], Γ is the vortex strength, l is the length of the vortex segment, and l_0 is the initial length of the vortex segment. Inside of r_{vc} , a Rankine vortex model was applied to desingularize the vortex.

Ramasamy suggests a r_0 value based on the chord length of the shedding blade section, but in practice, this approach can cause unintended side effects in VLMs. Testing showed that small enough time step sizes and panel sizes can cause the load calculation points (see Section 3.6) or collocation points of trailing edge panels to fall inside the vortex core radius of the latest row of wake vortex segments, leading to a perpetual under-prediction of forces. Instead, r_0 was set to an arbitrary constant value small enough to exclude any locations associated with the bound vorticity at which velocities must be calculated. The r_0 value used for the presented work was

$$r_0 = 0.25V_\infty dt \quad (3.2)$$

where dt is the time step size. In cases where a wake would intersect bound vorticity, a similar smoothing approach was applied to the bound vorticity except without any core radius growth over time. The bound vorticity was given a constant core radius equal to r_0 , which prevented unreasonably large influences when intersecting previously shed wakes while avoiding an unnecessary reduction of influence on the newest row of wake segments.

3.5 Slow-start Rev-up

The prescribed motion for a propeller is a constant rotation speed combined with a constant forward velocity. If such a motion were initiated impulsively, an abnormally strong

starting vortex would be created because of a lack of wake-induced downwash to reduce the effective angle of attack seen by the blade. This strong starting vortex causes increased wake deformation and must be sufficiently convected away from the propeller to achieve a steady-state solution. To alleviate the effects of the starting vortex, a slow-start rev-up scheme was implemented whereby the target rotation speed and forward velocity are achieved via a linear increase from much smaller values over a set number of revolutions (the studies presented here initiated at one percent of the target values and increased over two revolutions). Keeping the ratio of rotation speed to forward velocity constant keeps advance ratio constant and maintains the validity of the bound geometry and influence matrices, discussed in Section 3.2, over the course of the rev-up.

3.6 Load Calculation

Load calculation was performed using the Joukowski method, which gives the total force produced by the i^{th} chordwise and j^{th} spanwise panel, $\mathbf{F}_{i,j}^{tot}$, as the sum of a steady and an unsteady force component:

$$\mathbf{F}_{i,j}^{tot} = \mathbf{F}_{i,j}^{st} + \mathbf{F}_{i,j}^{unst} \quad (3.3)$$

The steady force component, $\mathbf{F}_{i,j}^{st}$, is given by

$$\mathbf{F}_{i,j}^{st} = \rho_{\infty}(\Gamma_{i,j} - \Gamma_{i-1,j})(\mathbf{U}_{i,j} \times \mathbf{l}_{i,j}) \quad (3.4)$$

where $\Gamma_{i,j}$ is the strength of the vortex ring associated with panel i, j , $\mathbf{l}_{i,j}$ is the vector of said ring's leading segment, and $\mathbf{U}_{i,j}$ is the local total velocity calculated at the midpoint of the leading segment. Equation 3.4, in effect, combines the steady force contributions of ring i, j 's leading segment and the upstream ring's trailing segment. For panels at the leading edge, the strength of the upstream ring, $\Gamma_{i-1,j}$, is set to zero. For panels at the trailing edge, the equation is unchanged, but note that there is no contribution from the

trailing segment because it is technically part of the wake and should be force-free.

Consistent with many other VLM implementations [69, 85], Equation 3.4 calculates the force from only the bound spanwise-oriented vorticity contained in the leading and trailing vortex segments. Such an approach derives from the assumption that the flow at any point along a blade is two-dimensional and normal to the spanwise direction. The bound chordwise-oriented vorticity of the side segments would then be aligned with the flow and produce no appreciable force. This assumption is generally valid for wings in forward flight or for propellers normal to the freestream but not necessarily for propellers at a nonzero angle of attack. For example, a blade at $\phi = 0^\circ$ or $\phi = 180^\circ$ on a propeller at $\alpha_p > 0^\circ$ is effectively at a negative angle of attack with respect to \mathbf{V}_∞ , and a vortex ring on the blade would be oriented with its side segments normal to \mathbf{V}_∞ . The leading and trailing segments will still account for a majority of the total force (being mostly normal to the dominant rotational velocity, $\boldsymbol{\omega} \times \mathbf{r}$) but the contribution from the side segments may not be negligible. Some references [95, 96] have suggested that unsteady VLMs should apply Equation 3.4 to all of the segments of a vortex ring for better accuracy. However, for the test case described in Chapter 4, load calculations that included steady force contributions from all bound vortex segments were less accurate than those made with the established spanwise-only method, especially for side and normal force.

The unsteady force component, $\mathbf{F}_{i,j}^{unst}$, is given by

$$\mathbf{F}_{i,j}^{unst} = \rho_\infty \frac{\partial \Gamma_{i,j}}{\partial t} A_{i,j} \frac{\mathbf{U}_{i,j} \times \mathbf{l}_{i,j}}{|\mathbf{U}_{i,j} \times \mathbf{l}_{i,j}|} \quad (3.5)$$

where $A_{i,j}$ is the area of panel i, j . According to Cole [69], there are two interpretations of the unsteady force component which agree in magnitude ($\rho_\infty \frac{\partial \Gamma_{i,j}}{\partial t} A_{i,j}$) but differ in directionality. The first is seen in a work by Drela [97] and is applied in the local lift direction, normal to the local total velocity; the second is seen in works such as [95, 96] and is applied in the panel normal direction. After testing both directions, applying the unsteady force component in the lift direction was found to produce more accurate results. These

findings support Katz and Plotkin's [87] remark that a normal force based solely on the pressure difference across the vortex ring overpredicts the induced drag by not capturing the suction peak.

When aggregating propeller forces, the individual force components can be summed and decomposed into directional components without regard for their point of application. When calculating propeller moments, the force components were applied at their respective leading segments' midpoints.

CHAPTER 4

MODEL EVALUATION

A series of studies were performed to evaluate RoBIN's accuracy and convergence characteristics with respect to simulation time, grid resolution, and time step resolution. The convergence studies were conducted using an isolated propeller geometry, and accuracy was tested for both an isolated propeller and a propeller upstream of a wing.

4.1 Geometry

The high-lift propeller (HLP) of the NASA X-57 Maxwell [98] was used as the test propeller because the exact geometry was known and CFD analyses of the blades without a spinner were readily available. The HLP has a radius of $R = 0.2880$ m, five blades with a constant MH 114 airfoil along the radius, and the geometry distributions shown in Figure 4.1 [99]. All studies were conducted at the HLP design condition of 4550 rpm, $V_\infty = 29.8$ m/s (58.0 kts), and $\rho_\infty = 1.225$ kg/m³ air density. The propeller origin about which moments were taken was defined as the intersection of the blade stacking axes and the rotation axis.

For the propeller and wing case, an airfoil cross section from the X-57 wing was extruded to form a rectangular wing. The wing has a span of 3.048 m (10.00 ft) and a chord of 0.7142 m (2.343 ft). The wing was positioned with its midspan quarter-chord at $[X, Y, Z] = [0.437315, 0, 0.108]$ m ($[1.43476, 0, 0.353]$ ft) relative to the propeller origin and with its chord plane parallel to the propeller's x - y plane. The midspan quarter-chord was the reference point for wing moments. Figure 4.2 shows the propeller and wing geometry as modeled in RoBIN.

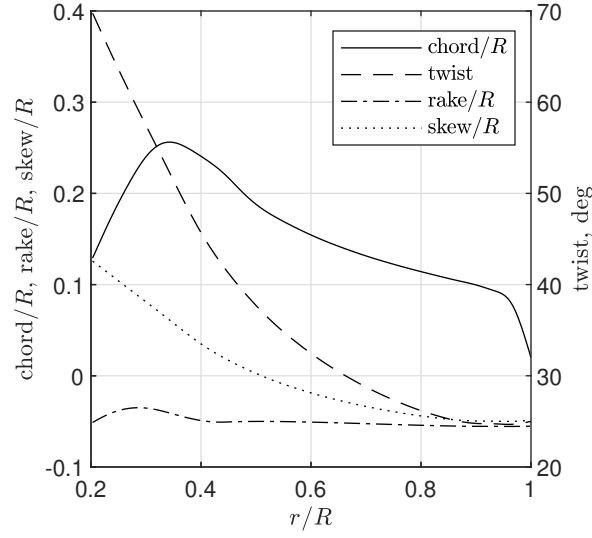


Figure 4.1: HLP blade geometry.

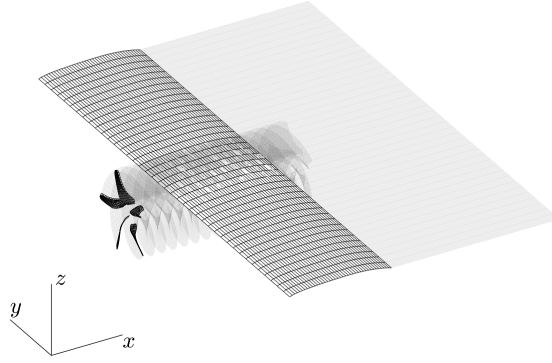


Figure 4.2: X-57 HLP and wing as modeled in RoBIN visualized with a notional prescribed wake.

4.2 Simulation Time Convergence

The first study investigated RoBIN's convergence behavior with respect to simulation time, measured in number of revolutions, N_{rev} . The geometry was discretized into 20 spanwise and chordwise panels per blade, and a time step size corresponding to $\Delta\phi = 5^\circ$ (72 steps per revolution) was chosen. Figure 4.3 shows the moving average of the forces and moments over the last revolution for a wide range of α_p . Although most runs converged smoothly, there exists an unsteadiness in the results that grows to a visually observable

magnitude by the $\alpha_p = 60^\circ$ case. The unsteadiness is due to increasingly strong distortions in the wake, as demonstrated in Figure 4.4. The inclusion of a vortex core model helped to avoid the worst of the singularity-related instabilities, but the wakes of loaded propellers will inevitably accumulate more curvature than what its fixed grid resolution can accurately model. This can lead to unrealistic stretching, improper wake intersection, and a general loss of geometric fidelity. Attaining cleaner convergence behavior at higher α_p would require a dynamic wake refinement algorithm. The study was repeated for coarser and finer grid and time step resolution settings with similar results.

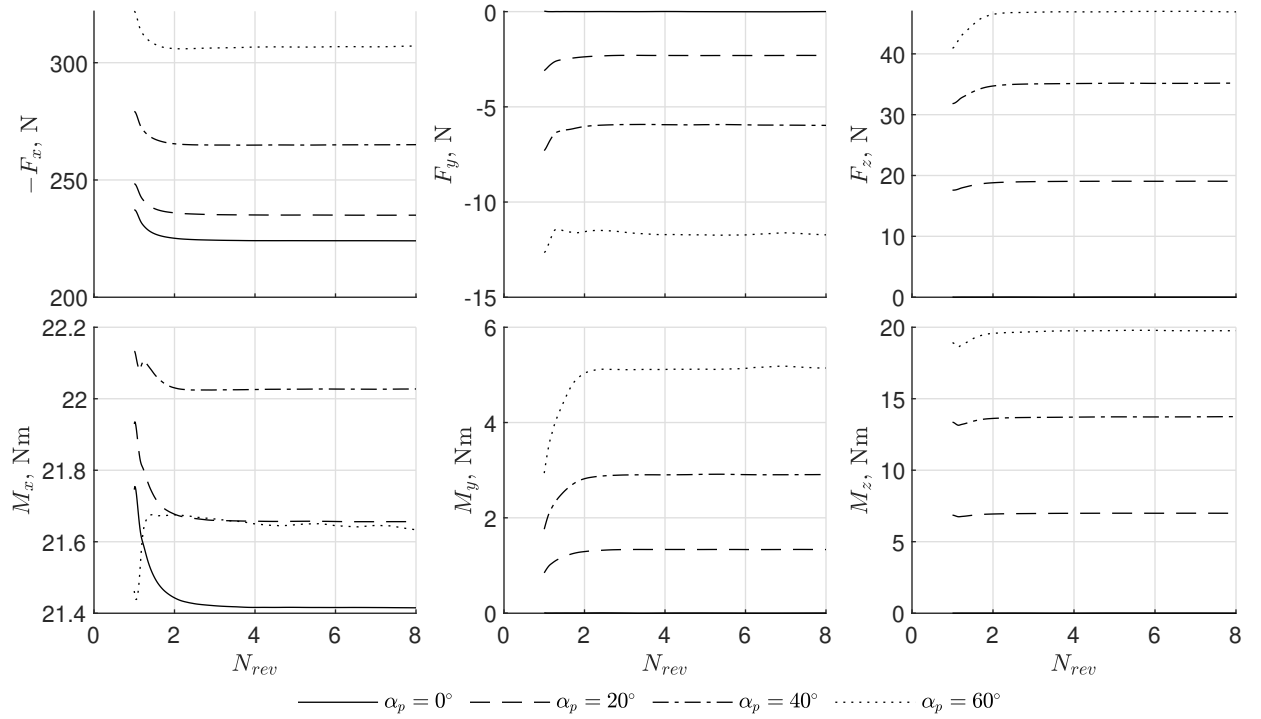


Figure 4.3: RoBIN convergence behavior with respect to number of revolutions.

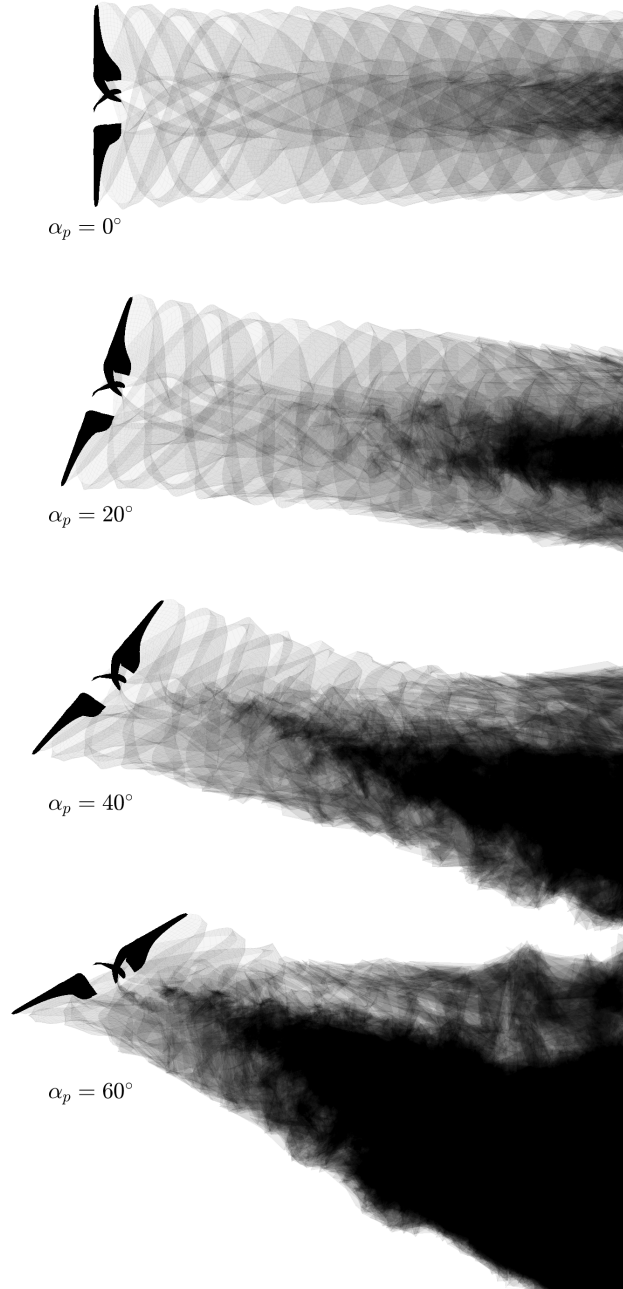


Figure 4.4: Demonstration of increasingly strong wake distortions with propeller angle of attack.

4.3 Grid Resolution and Time Step Resolution Convergence

The second study investigated RoBIN's convergence behavior with respect to grid resolution and time step resolution. Grids were constrained to have the same number of chordwise and spanwise panels, and the time step sizes were constrained to result in a whole number

of steps per revolution. Figure 4.5 shows the convergence behavior with respect to grid resolution, measured in number of panels per blade, N_{ppb} , and Figure 4.6 shows the convergence behavior with respect to time step resolution, measured in number of time steps per revolution, N_{tpr} . The values shown are for $\alpha_p = 30^\circ$ and are the average forces and moments over the last revolution normalized by their respective CFD predictions, denoted by an asterisk (CFD results are discussed in Section 4.4).

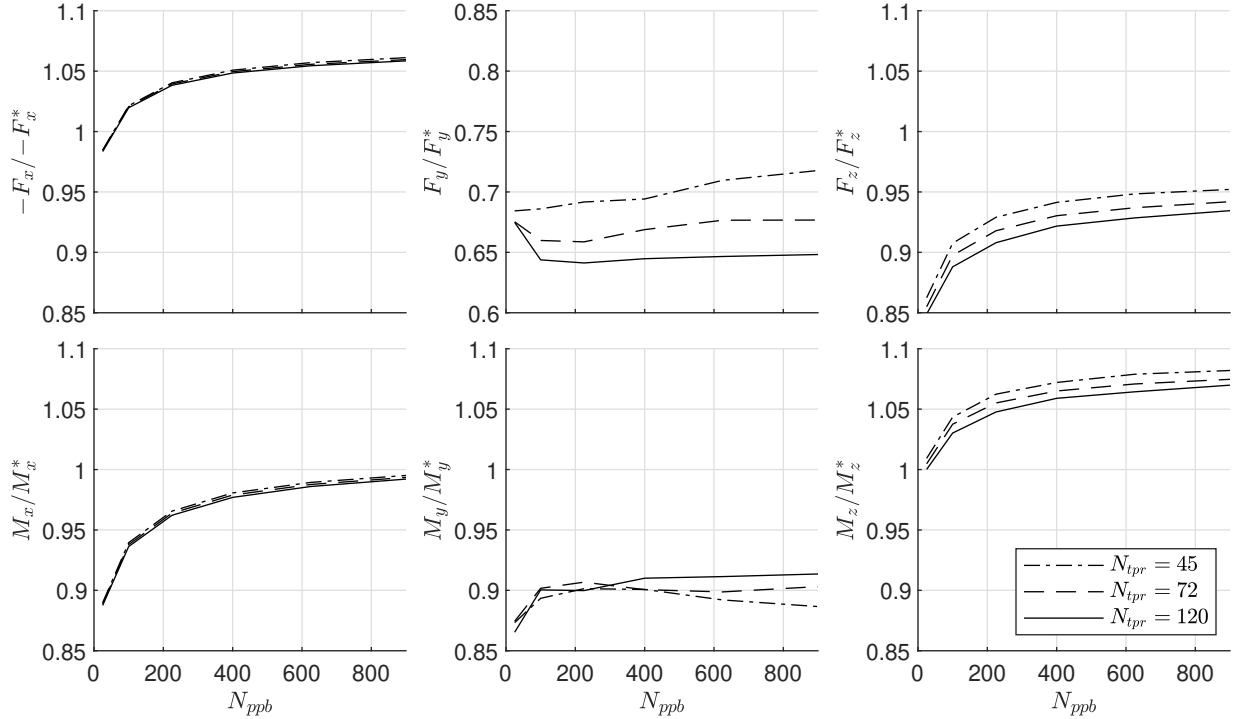


Figure 4.5: RoBIN convergence behavior with respect to grid resolution. $\alpha_p = 30^\circ$.

Overall, the convergence is well behaved with most metrics asymptoting towards values within 10% of the CFD predictions. F_y and M_y show the most difficulty in converging with both measurements seeming to fluctuate from what would be a smooth convergence curve. Upon closer inspection, these fluctuations are present for all other forces and moments but are imperceptible when compared to the magnitudes of their unnormalized values. Based on this observation, these fluctuations are likely caused by the same wake distortions discussed in Section 4.2 because F_y and M_y are primarily caused by a wake-induced velocity asymmetry that, unlike F_z and M_z , is not diluted by the asymmetry in tangential freestream

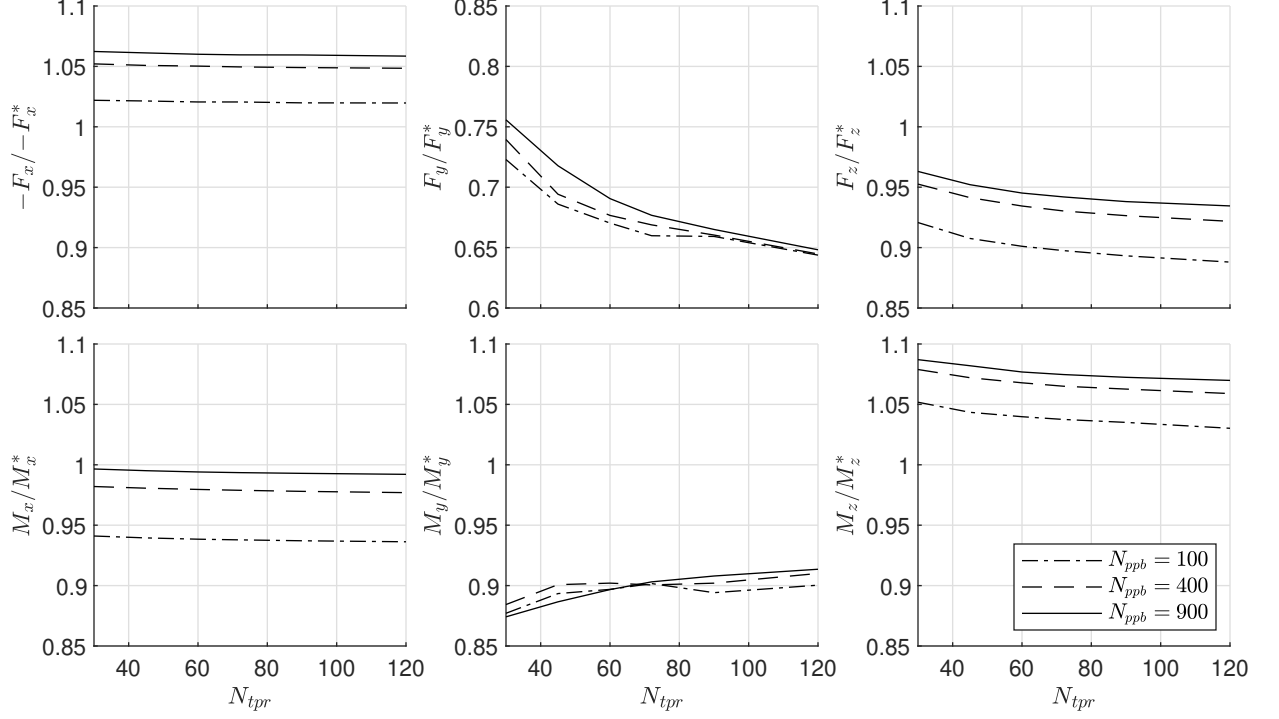


Figure 4.6: RoBIN convergence behavior with respect to time step resolution. $\alpha_p = 30^\circ$.

velocity. The 25-35% underprediction in F_y is due to the small magnitude of F_y^* . The impact of any inaccuracy, such as the lack of viscous drag, is exaggerated in the prediction of F_y .

F_x and M_x are especially insensitive to N_{tpr} because increasing N_{tpr} has little effect on the total amount of vorticity in the wake and, therefore, little effect on the average velocity induced by the wake at the propeller disk. The increase in each measurement with N_{ppb} is at least partly due to the inset distance shrinking as the panel size decreases, resulting in larger modeled blade areas.

4.4 Accuracy Compared to CFD

RoBIN's accuracy was evaluated by comparing against CFD analyses. The primary reason for using CFD instead of experimental data was the ability to exclude the nacelle and spinner, which have been shown to generate side and normal forces comparable in magnitude to those of the blades [100]. Since the mean camber surface representation in VLMs

is unsuitable for modeling thick bodies, a blade-only geometry was more appropriate for evaluating RoBIN's accuracy. The CFD software used for the evaluation was OVERFLOW. In addition to the results presented in this section, a test case of the isolated HLP in forward flight at zero angle of attack can be found in Appendix B.

4.4.1 OVERFLOW Setup

The model geometries were created using Open Vehicle Sketch Pad (OpenVSP) [101] and exported in a PLOT3D format for gridding. Chimera Grid Tools (CGT) [102] was used to assemble the overset grid systems. The final grid systems were saved as unformatted, double-precision, big endian multigrid files for analysis in OVERFLOW.

OVERFLOW (OVERset grid FLOW solver) is a structured, overset grid, Reynolds-Averaged Navier-Stokes, CFD flow solver developed at NASA [103, 104]. A fifth-order WENO5M (Weighted Essentially Non-Oscillatory) method [105] with HLLE++ (Harten, Lax, van Leer and Einfeldt) flux scheme [106] was used to calculate inviscid flux contributions and second-order central differences were used to approximate the viscous flux. A $k-\omega$ SST-RC-QCR2000 (rotation correction with quadratic constitutive relationship) turbulence model [107, 108] coupled with the Langtry-Menter CFX-v-1.1 transition model [109], despite not being Galilean invariant, was used according to best practices for the X-57 model, as documented in [98, 99]. This method has been successfully used in other situations with rotational reference frames, e.g., Jain [110, 111]. The propeller analyses used dual time stepping with 20 subiterations and a physical step size corresponding to 1° of rigid body rotation to predict the time accurate flow field, with at least eight revolutions of propeller travel being simulated. Total forces and moments were then averaged over the final revolution.

To obtain sectional force distributions over the propeller disk, solution files were generated every 12 degrees following the eighth propeller revolution. The sectional forces were computed along each blade at each azimuthal position using the TRILOAD program [112],

which slices a triangulation of surface loads into bins defined by a binning direction and distance. Blade sectional loads were computed using 100 bins uniformly spaced along the radial direction between the blade root and tip.

4.4.2 Angle of Attack Sweep for Isolated Propeller

Figure 4.7 shows the comparison of RoBIN vs. OVERFLOW isolated propeller results over a sweep of α_p . Simulation settings were selected based on the results of the convergence studies—the geometry was discretized into 20 spanwise and chordwise panels per blade ($N_{ppb} = 400$), the time step size corresponded to $\Delta\phi = 5^\circ$ ($N_{tpr} = 72$), and the simulations were run until $N_{rev} = 6$.

RoBIN’s predictions show good agreement with those from OVERFLOW until stall begins to occur in the OVERFLOW solutions at $\alpha_p = 40^\circ$. The stall occurs in the upwind region, and the loss of lift there causes a sharp departure in predicted M_y and a corresponding departure in predicted $-F_x$. Prior to stall occurring, $-F_x$ predictions from RoBIN are approximately 5% larger than OVERFLOW’s predictions. This overprediction is likely due to a combination of lacking viscous drag in the axial direction and a discrepancy between the inviscid and viscous lift curve characteristics of the MH 114 airfoil. As shown in Figure 4.8, the viscous lift curve of the MH 114 airfoil is slightly lower than the inviscid lift curve¹ due to Reynolds number effects. The viscous lift curve also gradually stalls so regions of the blades at $\alpha_{eff} \gtrsim 5^\circ$ overpredict lift and, consequently, thrust more in RoBIN. The discrepancy in lift curves also causes RoBIN’s M_z predictions to be approximately 5% higher than those from OVERFLOW. Since the advancing blades experience higher α_{eff} than the retreating blades, the advancing side sees a greater overprediction of thrust, resulting in a higher M_z prediction from RoBIN.

RoBIN’s underprediction of F_z is not entirely unwelcome. The recognized lack of viscous drag effects in RoBIN should result in an underprediction of F_z because the presence

¹The inviscid lift curve was generated by modeling a wing with an aspect ratio of 1000 and extracting the forces from the middle section.

of a $V_{\infty,z}$ component in the $+z$ direction would produce a corresponding net parasitic drag force in OVERFLOW. RoBIN's F_y predictions are also thought to be reasonable considering the lack of viscous effects.

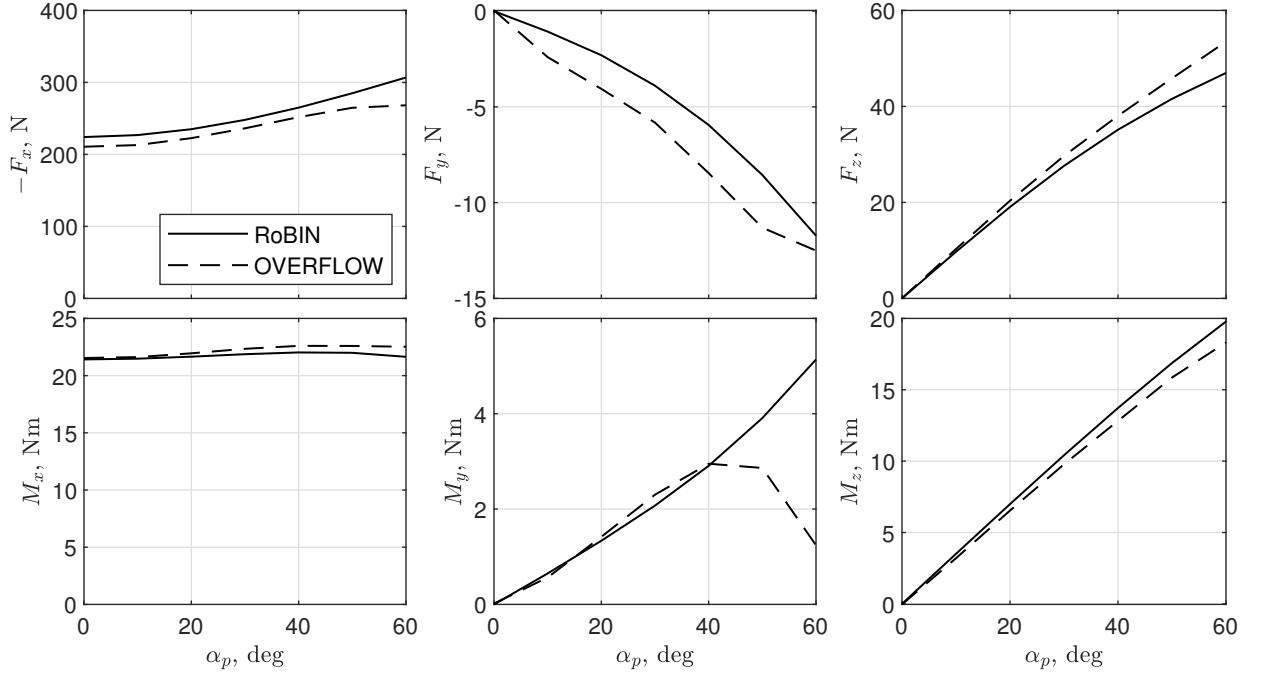


Figure 4.7: Comparison of RoBIN and OVERFLOW results for the isolated HLP over a sweep of α_p .

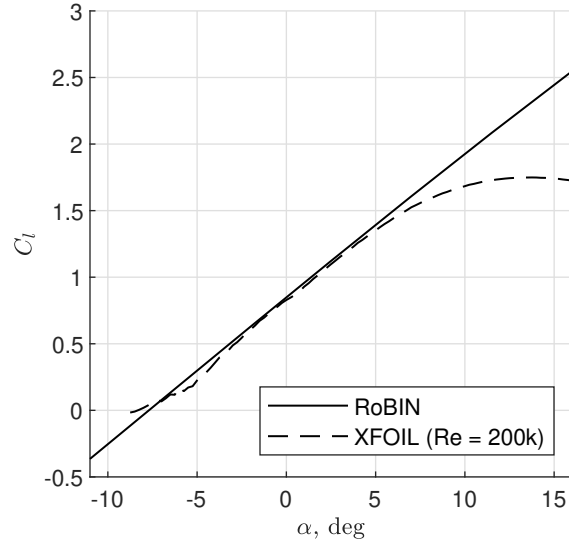


Figure 4.8: Comparison of inviscid (RoBIN) and viscous (XFOIL) lift curves for the MH 114 airfoil.

4.4.3 Force Distribution Comparisons

For a more in-depth analysis of the errors observed, Figure 4.9 compares contours of sectional thrust, $-F'_x$ and $-F'^*_x$, from RoBIN and OVERFLOW, respectively, overlaid on a colored map of the dimensional error, $-F'_x - (-F'^*_x)$ for $\alpha_p = 30^\circ$. The extra lift resulting from the inviscid lift curve discussed previously is evident by the general overprediction over most of the disk, and the enlarged RoBIN contours on the advancing side confirm that the discrepancy is more pronounced there. Interestingly, the region of highest (dimensional) error—the tip region between approximately $\phi = 30^\circ$ and $\phi = 90^\circ$ —is not aligned with the peak loading direction of $\phi \approx 105^\circ$, indicating that its cause is likely not related to the discrepancy in lift curves. Figure 4.10 shows the same $-F'_x$ and $-F'^*_x$ contours as Figure 4.9 but overlaid on a colored map of the normalized error, $\frac{-F'_x - (-F'^*_x)}{-F'^*_x}$. When normalized, the region of highest error is revealed to be a band of overprediction at the tip between $\phi = 270^\circ$ and $\phi = 90^\circ$. Note that the blank area near the root is due to $-F'^*_x$ going to zero and the normalized error exceeding the colorbar limits, rather than being a region of zero error.

The cause for this band of overprediction is thought to be explained by Figure 4.11, which shows the component of kinematic velocity (i.e., velocity due to rotation and forward motion) in the spanwise direction² over a blade at a selection of azimuthal positions. Note the outward velocity at the blade tips in the downwind region; this crossflow is a result of the $V_{\infty,z}$ velocity component. In reality, outward crossflow at the tip would cause wake shedding off of the blade tip as if it were a trailing edge, but such shedding is not realized in RoBIN because wake shedding is prescribed only along the trailing edge. The lack of shedding at the tips is suspected to result in less downwash on and exaggerated lift from the adjacent blade sections. That the overprediction is a relatively constant percentage of $-F'_x$ at the tip supports the hypothesis of a wake-related inaccuracy because the strength

²The spanwise direction is not the same as the radial direction. The spanwise direction is normal to the blade root and tip edges and is the same across the entire blade for a given ϕ . In contrast, the radial direction points toward the propeller origin and would vary over a blade.

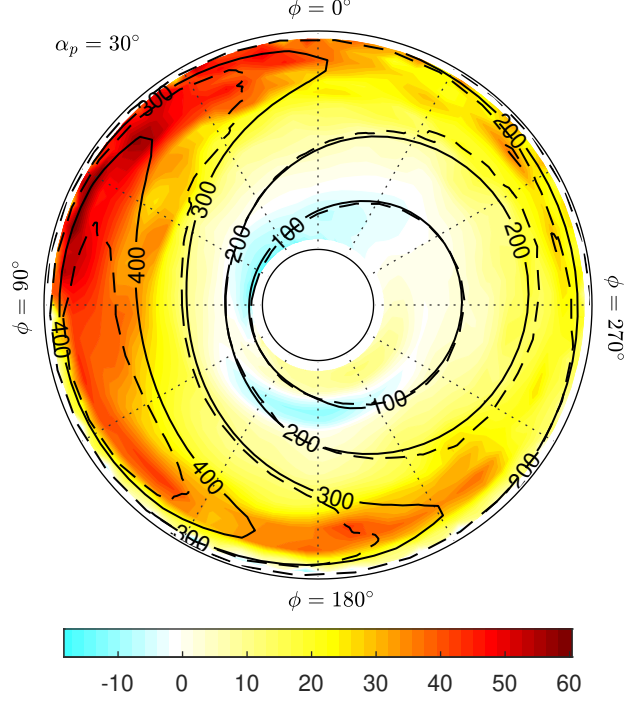


Figure 4.9: Contours of $-F'_x$ and $-F'^*_x$ at $\alpha_p = 30^\circ$ overlaid on a colored map of the dimensional error. Solid contours are from RoBIN and dashed contours are from OVERFLOW.

of the wake shed, and therefore the strength of the downwash, is proportional to the lift. A similar tip-shedding effect should occur with the inward crossflow at the blade roots in the upwind region. However, $-F'^*_x$ is near zero here so it is difficult to assess whether the errors are due to modeling inaccuracy or divide-by-zero exaggeration.

Figure 4.12 shows a plot of F'_y , F'^*_y , and the dimensional error, $F'_y - F'^*_y$, and Figure 4.13 shows a similar plot of F'_z , F'^*_z , and $F'_z - F'^*_z$. In both instances, good agreement is found between the RoBIN and OVERFLOW contours with peak errors occurring in the root region, where the blade has the highest chord length. The peak errors for both forces are also consistent with a lack of viscous drag—in Figure 4.12, the leftward sweeping blade on the downwind side lacks a viscous drag force in the $-y$ direction, and in Figure 4.13, the downward sweeping blade on the advancing side lacks a viscous drag force in the $+z$ direction. Normalized error plots are not shown for F'_y and F'_z because there were widespread regions of near-zero F'^*_y and F'^*_z that made the plots ineffective.

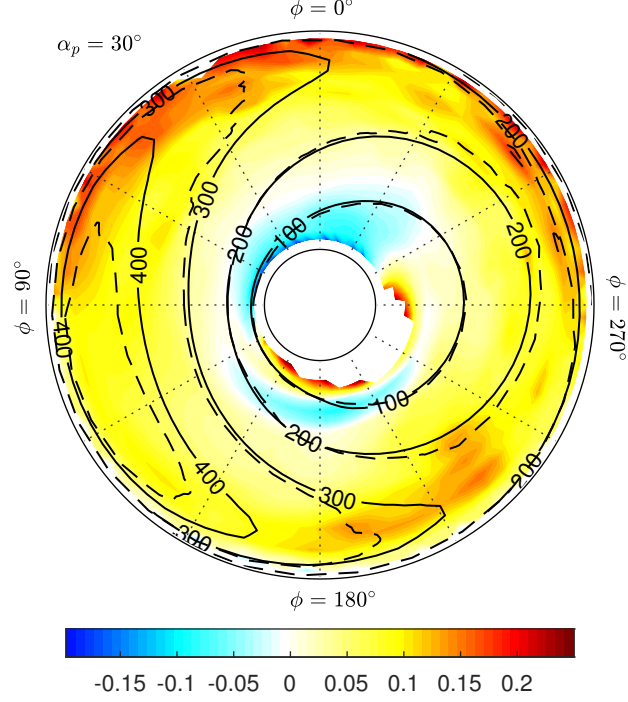


Figure 4.10: Contours of $-F'_x$ and $-F'^*_x$ at $\alpha_p = 30^\circ$ overlaid on a colored map of the normalized error. Solid contours are from RoBIN and dashed contours are from OVERFLOW.

4.4.4 Angle of Attack Sweep for Propeller and Wing

For the propeller and wing case, the propeller geometry was discretized into 15 spanwise and chordwise panels per blade ($N_{ppb} = 225$), and the wing was discretized into 40 spanwise and chordwise panels. The time step size corresponded to $\Delta\phi = 7.2^\circ$ ($N_{tpr} = 50$), and the cases were run until $N_{rev} = 8$. The simulation time was increased to allow the propeller wake to propagate to about six revolutions behind the wing, and the time step and grid resolutions were coarsened to maintain a runtime comparable to that of the isolated propeller case. The range of α_p was reduced to $0^\circ \leq \alpha_p \leq 30^\circ$ because RoBIN is not capable of predicting the wing stall that occurs for $\alpha_p \gtrsim 15^\circ$.

Figure 4.14 shows the comparison of the propeller forces and moments with results from the isolated case included for reference. That OVERFLOW's $-F_x$ and M_x results are higher in the presence of the wing than in the isolated case is likely because of the blockage effect from the 18% thick wing. RoBIN's $-F_x$ and M_x results do not show this increase

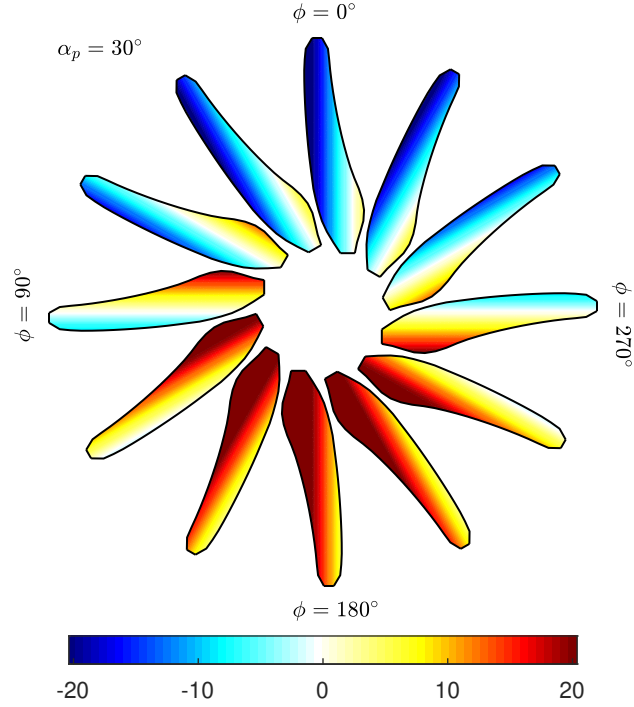


Figure 4.11: Shaded map of the component of kinematic velocity in the spanwise direction over a blade at various azimuthal positions. Positive values defined as inward toward the center.

and are nearly identical to isolated results because the thin vortex lattice representation of the wing does not produce thickness effects. Good agreement is seen for M_y , which approximately doubles with the wing's presence. The overprediction at $\alpha_p = 0^\circ$ is also attributed to the lack of blockage effects. Since the wing is positioned behind the upper (downwind) half of the propeller disk, the presence of blockage would increase thrust there and add a negative pitching moment that is not captured in RoBIN. As α_p increases, the wing blockage is projected further down the disk (toward the upwind side) so the negative pitching moment would decrease. The increases in F_z and M_z from isolated results indicate the presence of upwash from the wing, which increases the effective angle of attack observed by the propeller. The change in effective angle of attack can be estimated from the horizontal shift between the interacting and isolated results and is relatively consistent between F_z and M_z over the range of α_p . For example, both F_z and M_z at $\alpha_p = 10^\circ$ in the presence of the wing are approximately equal to F_z and M_z at $\alpha_p = 15^\circ$ in isolation.

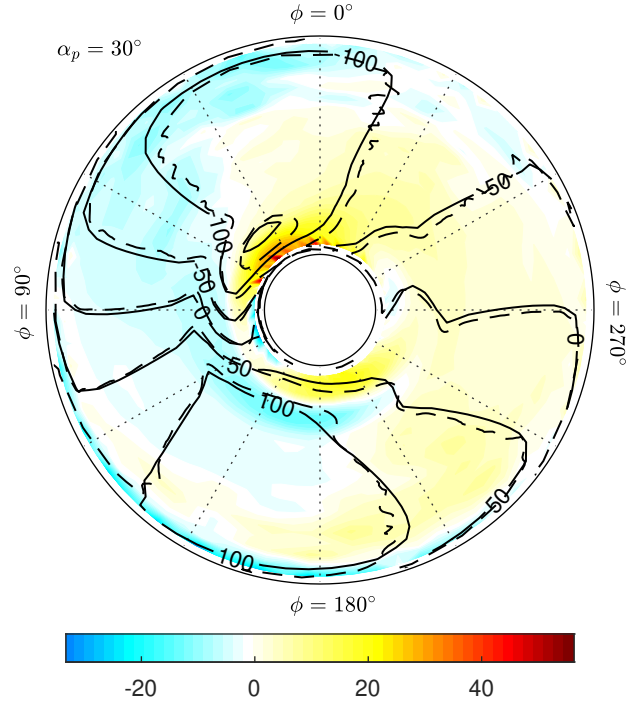


Figure 4.12: Contours of F'_y and F'^*_y at $\alpha_p = 30^\circ$ overlaid on a colored map of the dimensional error. Solid contours are from RoBIN and dashed contours are from OVERFLOW.

Figure 4.15 shows the comparison of the wing forces and moments for completeness. The wing forces and moments were not expected to be as accurate as those of the propeller because the propeller wake passing through the wing allows many opportunities for exaggerated panel forces. If a wake vortex segment passes closely to a load calculation point on the wing, the vortex segment may induce an unrealistically high velocity (even with the vortex core model), leading to an exaggerated force from the respective bound segment. The inconsistency in the moment predictions, which are most sensitive to local peak loads, seem to reflect this problem. The lift and drag forces are less sensitive to local peak loads and trend closer with OVERFLOW results, and the drag is understandably underpredicted due to a lack of viscous effects. The sudden change in RoBIN trends between $\alpha_p = 20^\circ$ and $\alpha_p = 30^\circ$ is believed to be a result of some of the propeller wake leaking through the wing surface rather than deflecting to flow along the surface. The reduction in lift, drag, and pitching moment magnitudes are all consistent with this explanation. The error could

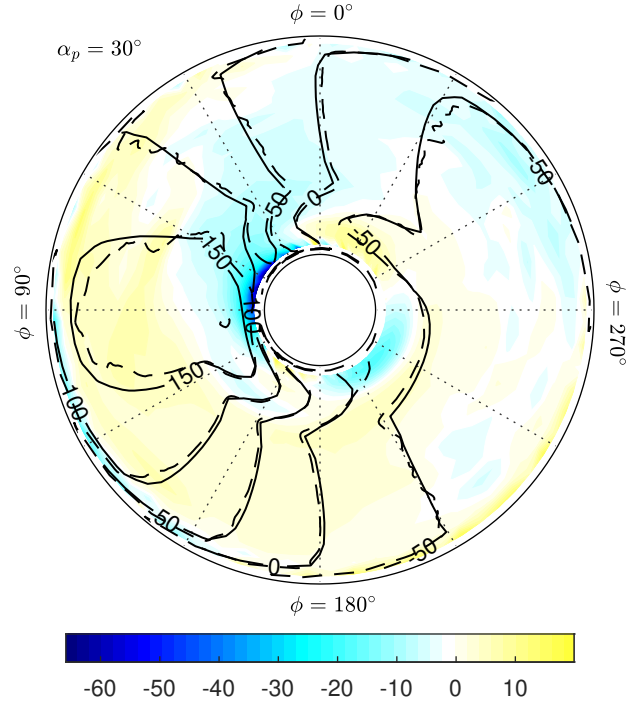


Figure 4.13: Contours of F'_z and F'^*_z at $\alpha_p = 30^\circ$ overlaid on a colored map of the dimensional error. Solid contours are from RoBIN and dashed contours are from OVERFLOW.

be reduced by increasing either the wing grid or time step resolution.

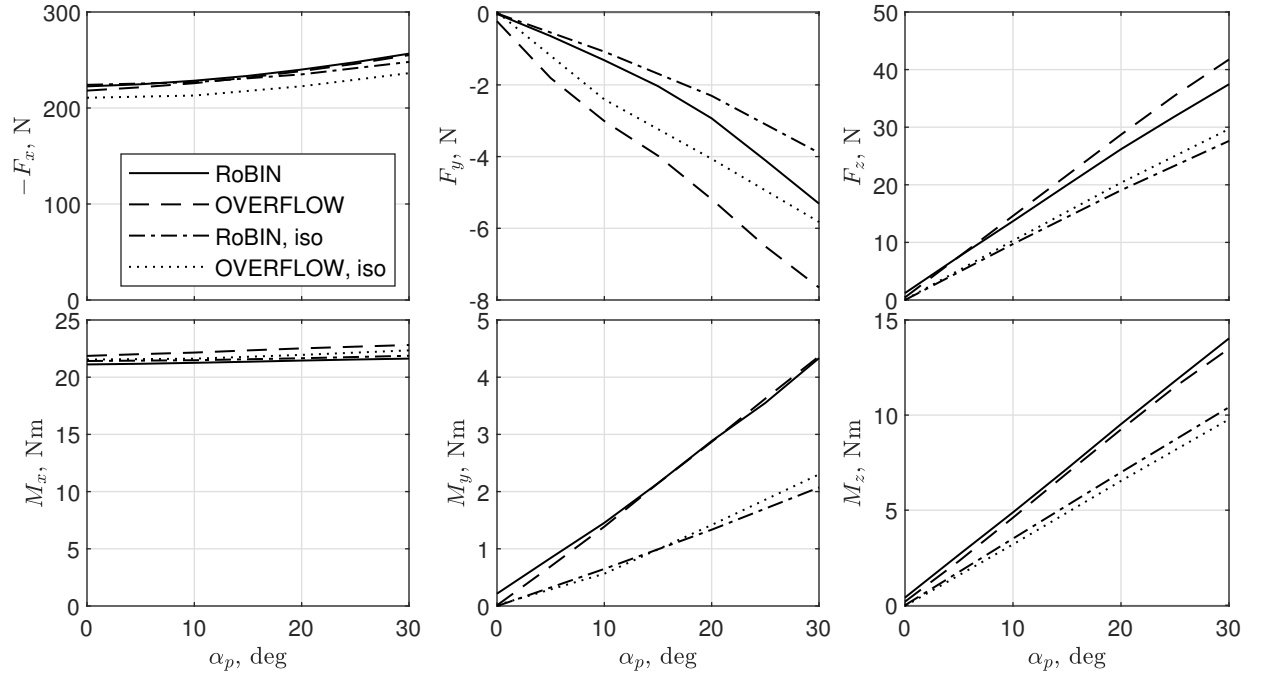


Figure 4.14: Comparison of RoBIN and OVERFLOW results for the propeller in the propeller and wing case over a sweep of α_p with isolated propeller results included.

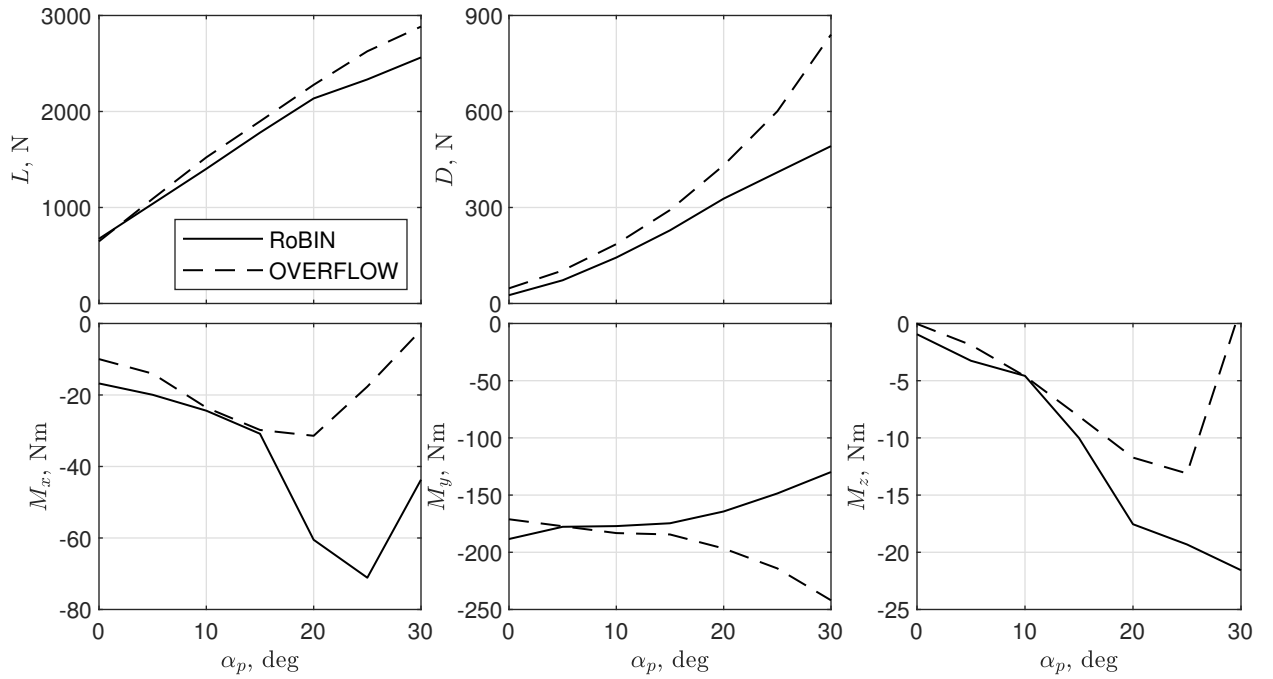


Figure 4.15: Comparison of RoBIN and OVERFLOW results for the wing in the propeller and wing case over a sweep of α_p .

4.5 Computation Time

Since the RoBIN and OVERFLOW results presented here were generated using different computing resources, we will avoid a rigorous comparison and only give an anecdotal account of the computation time. The RoBIN cases were run in sequence on a server with two Intel Xeon Platinum 8160 CPUs, but the Biot-Savart calculations were accelerated via four NVIDIA Tesla P4 GPUs. In the study of grid and time step resolution, the runtimes ranged from 20 seconds to 170 minutes per case. The resolution settings that were selected for the subsequent isolated propeller analyses (400 panels per blade and 72 time steps per revolution) required about 20 minutes per case. The OVERFLOW cases were run in parallel on the NASA Langley Research Center K3-subcluster using 16 Intel Xeon Processor E5-2670 CPUs for each case. The OVERFLOW cases all completed in about 60 hours.

CHAPTER 5

INVESTIGATING THE CAUSES OF PROPELLER PITCHING MOMENT

In this chapter, we will use RoBIN to test the hypotheses derived in Chapter 2. Each hypothesis was tested by enabling and disabling the suspected source of induced velocity asymmetry and tracking the contribution of said source to the induced velocity observed at the blades.

Although the X-57 HLP validation cases showed that propeller pitching moment could be modeled accurately, the relatively complicated geometry made it difficult to isolate the hypothesized induced velocity effects for testing. Instead, a set of simplified propeller and wing geometries are used to test the effects of a skewed wake and wing circulation on propeller pitching moment.

5.1 Geometry

The propeller geometry used is based on Leishman’s ideally twisted rotor for hover [113], which is defined by a constant blade chord and the twist distribution,

$$\theta(r) = \frac{\theta_{tip}}{r/R} \quad (5.1)$$

where θ_{tip} is the blade twist at the tip. In reality, a VTOL propeller would most likely need a variable pitch mechanism to be efficient over the widely varying conditions between hover and forward flight. Thus, a collective pitch was added to Equation 5.1 to give

$$\theta(r) = \frac{\theta_{tip}}{r/R} + \theta_{coll} \quad (5.2)$$

For the following isolated propeller cases, $\theta_{tip} = 7^\circ$, $\theta_{coll} = 5^\circ$, and $R = 0.5$ m. The propeller has two blades of constant $0.15R$ chord that are constructed from flat plate airfoils

stacked at the quarter-chord. No spinner was included but a hub cutout extending out to $0.2R$ was applied. The design operating condition was selected to be 3600 rpm at $V_\infty = 30$ m/s, which corresponds to an advance ratio of $J = 0.5$. For the propeller and wing cases, the same propeller was positioned in front of a rectangular 5 m span by 0.1 m chord wing with flat plate airfoils. The wing was centered behind the propeller with the wing's quarter-chord $1R$ away from the propeller origin in the x direction and with the wing's chord plane (initially) parallel to the propeller's x - y plane.

The propeller blades were modeled with 20 spanwise panels each, the wing was modeled with 40 spanwise panels, and both the propeller blades and wing were modeled with a single row of chordwise panels. This single row of chordwise panels combined with the quarter-chord offset of the bound vortex rings from the physical geometry grid (as described in Section 3.1) meant that the leading edges of the bound vortex rings would be aligned along the surfaces' quarter chords, similar to a lifting line model. A simple lifting line-like model has two advantages here. First, since we are interested in the influence of induced velocities on blade forces, which are generated by only the leading edge segments of the bound vortex rings, we can probe the exact induced velocities along the single row of lifting vortex segments and avoid having to derive a chordwise average. Second, since wing circulation can be increased in several ways (chord, camber, angle of attack), a lifting line-like representation allows us to focus on the effect of changing circulation without having to worry about the variations in the distribution of vorticity associated with changes in wing geometry. Similar reasoning is behind the selection of a very short wing chord. The wing's circulation will be controlled by adjusting the wing inclination, and the short chord reduces the amount of variation in the wake-shedding location at the trailing edge. The propeller and wing, as modeled in RoBIN, are illustrated in Figure 5.1.

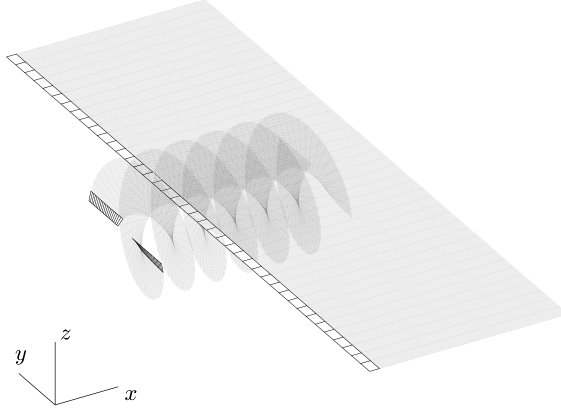


Figure 5.1: Generic propeller and wing as modeled in RoBIN visualized with a notional prescribed wake.

5.2 Testing the Effect of a Skewed Propeller Wake

To isolate the effect of a skewed wake on the propeller pitching moment of an isolated propeller, an ad hoc prescribed wake mode was added to RoBIN. The prescribed wake mode solved for the wake strength as usual but forced the wake to propagate as axisymmetric helices in the $+x$ direction at a velocity of $V_\infty \cos(\alpha_p)$. This prescribed wake should, in effect, create an induced velocity distribution at the propeller disk that is asymmetric across the z axis (due to the advancing-retreating blade effect) but symmetric about the y axis, similar to the induced velocity distribution used by Ribner [13]. A sweep was conducted over $0^\circ < \alpha_p < 60^\circ$ and each simulation was run for eight revolutions with 72 time steps per revolution.

Figure 5.2 compares the propeller forces and moments resulting from the prescribed wake and free wake modes. The results show why early propeller induced velocity models that did not capture skewed-wake effects still tended to be useful; the prescribed wake predictions of $-F_x$, M_x , F_z , and M_z agree relatively well with those of the free wake, especially at lower α_p where conventional propellers would operate. However, the prescribed wake mode severely underpredicted M_y and F_y , which are nonzero only because the helical

wake geometry was not symmetric about the x - y plane.

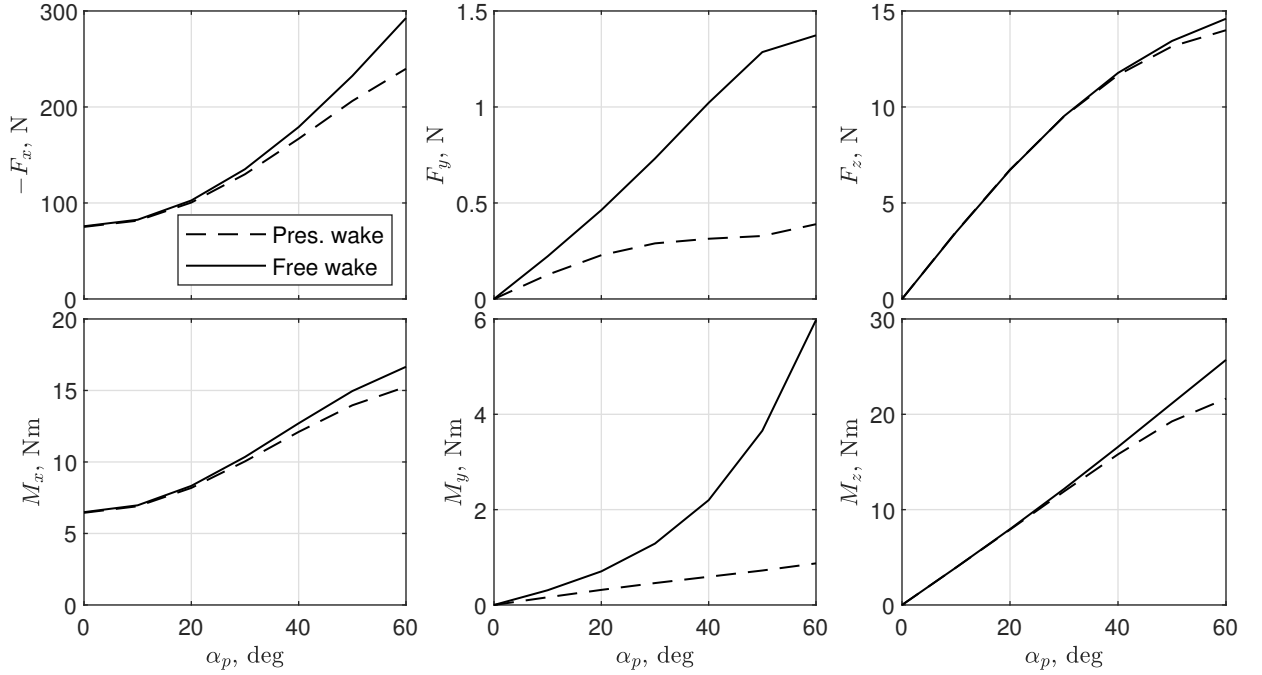


Figure 5.2: Comparison of propeller forces and moments over a sweep of α_p using prescribed wake and free wake modes.

For a more in-depth analysis, Figure 5.3 compares the x component of the total induced velocity (due to both bound and wake vortex rings) observed along the blades over the course of the last revolution from the prescribed and free wake modes at $\alpha_p = 30^\circ$. As expected, the prescribed wake mode resulted in a distribution that is nearly symmetric about the y axis. The free wake mode resulted in noticeably lower induced velocities on the upwind half of the disk. To better illustrate the difference, Figures 5.4 and 5.5 decompose the axial induced velocity into contributions from the bound and wake vortex rings, respectively. The bound contributions show relatively little difference whereas the wake contributions are clearly more negative on the upwind half of the disk in the free wake mode. Overall, these results support our hypothesis that the skewed wake effect is the primary cause of propeller pitching moment for an isolated propeller.

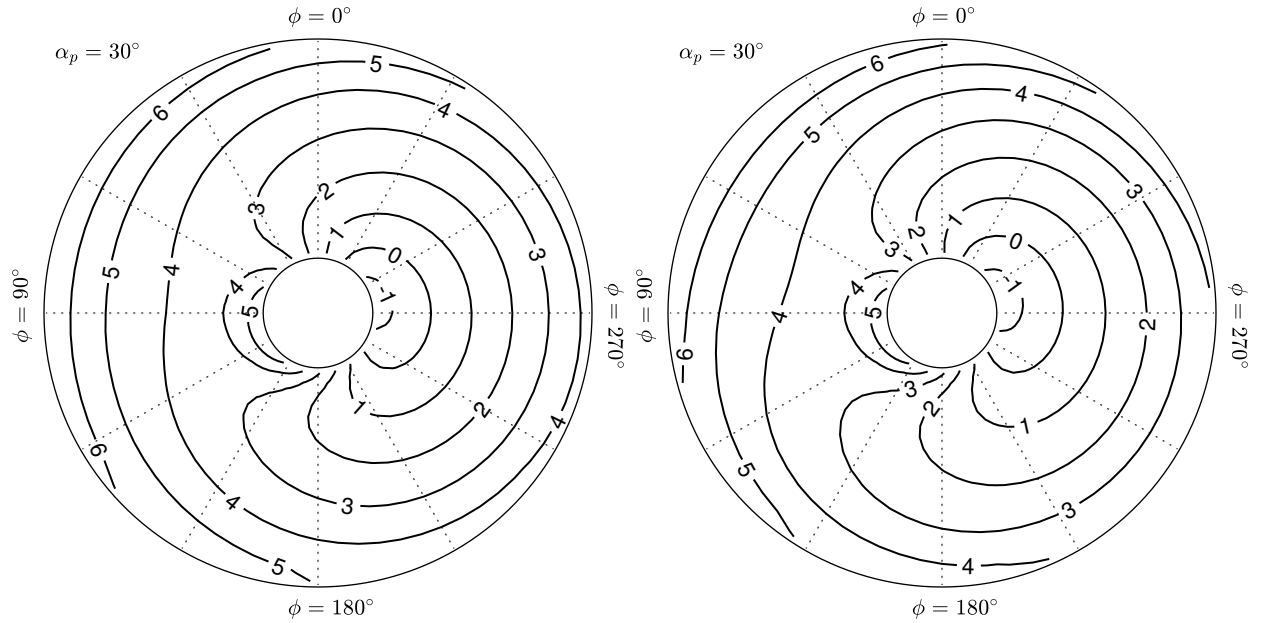


Figure 5.3: Contours of total axial induced velocity observed by the blades over the last revolution at $\alpha_p = 30^\circ$. Prescribed wake mode (left) and free wake mode (right).

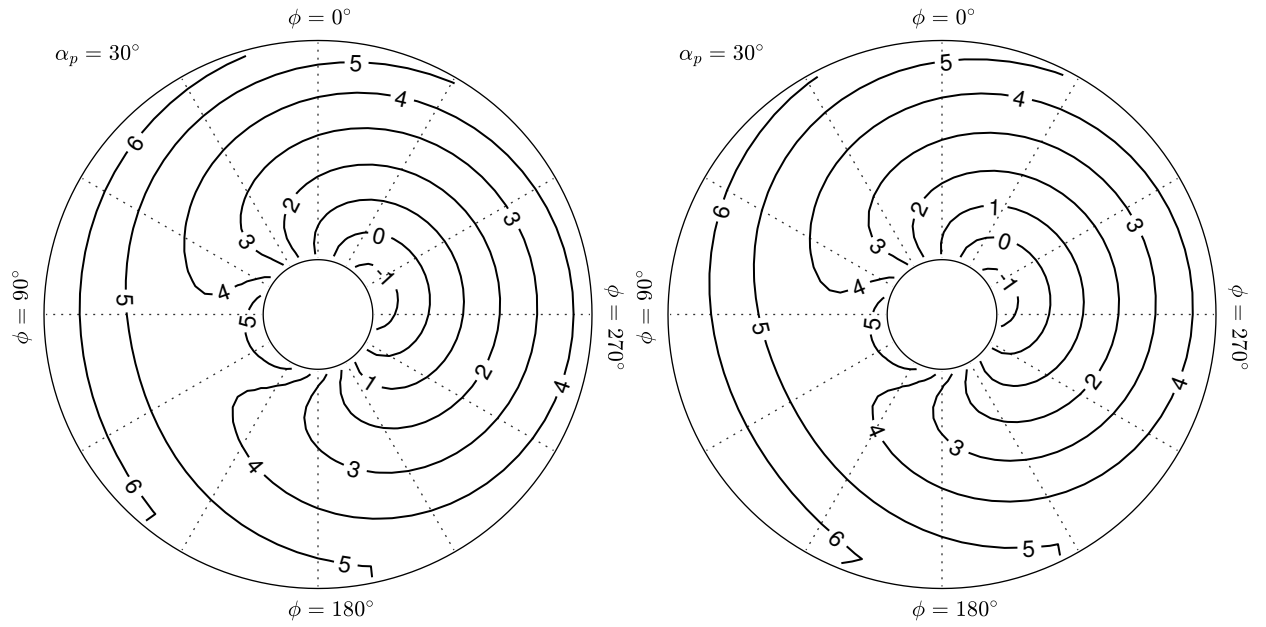


Figure 5.4: Contours of bound vortex rings' contribution to axial induced velocity observed by the blades at $\alpha_p = 30^\circ$. Prescribed wake mode (left) and free wake mode (right).

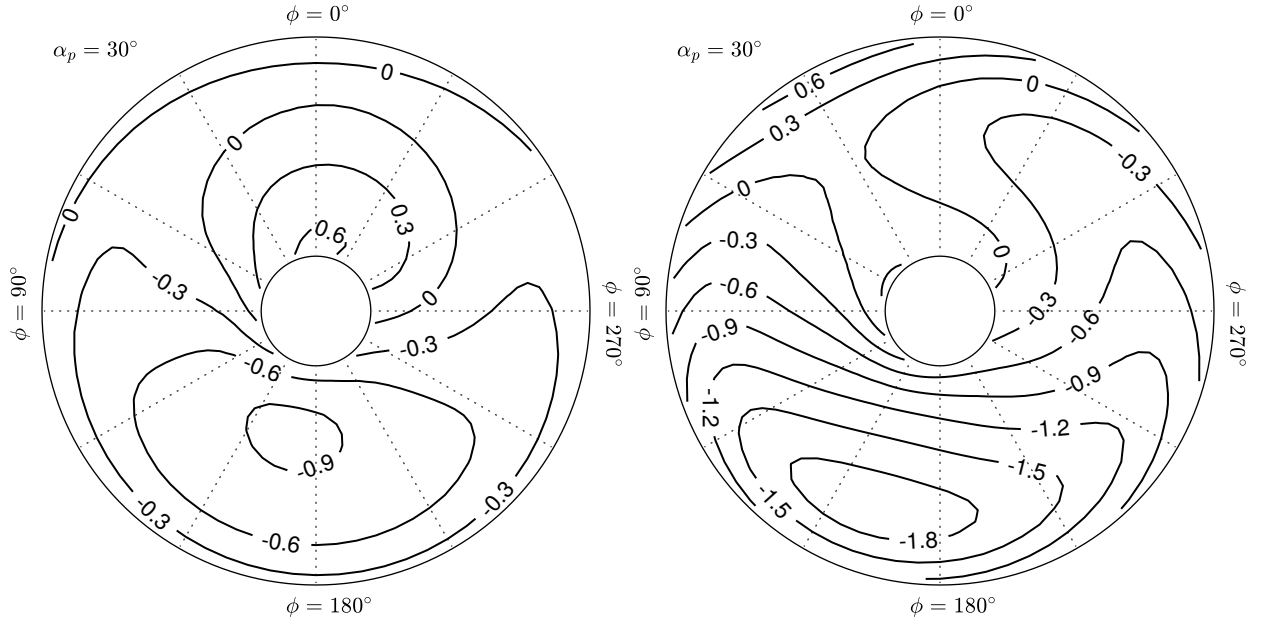


Figure 5.5: Contours of wake vortex rings' contribution to axial induced velocity observed by the blades at $\alpha_p = 30^\circ$. Prescribed wake mode (left) and free wake mode (right).

5.3 Testing the Effect of Wing Circulation

To test the effect of wing circulation, the wing was independently inclined about its quarter-chord to $i_w = 0^\circ, 10^\circ$, and 20° , which resulted in lift-to-thrust ratios of 0, 3.8, and 7.5, respectively, when $\alpha_p = 0^\circ$. A sweep of $0^\circ \leq \alpha_p \leq 30^\circ$ was performed at each i_w with each simulation running for 10 revolutions at 40 time steps per revolution. Figure 5.6 shows the propeller forces and moments from these sweeps. Aside from the clear increases in F_y and M_y , increases in wing circulation have almost no effect on the other forces and moments. Only minute increases in F_z and M_z are observed, which is consistent with an increase in effective α_p induced by the wing's upwash.

Figure 5.7 shows the total axial induced velocity observed along the blades with the wing at $i_w = 0^\circ$ and 20° , respectively. The increase in i_w is seen to shift the contours up-stream such that the upstream half of the disk experiences less downwash than the down-wind half, consistent with the increase in pitching moment seen in Figure 5.6. Figures 5.8

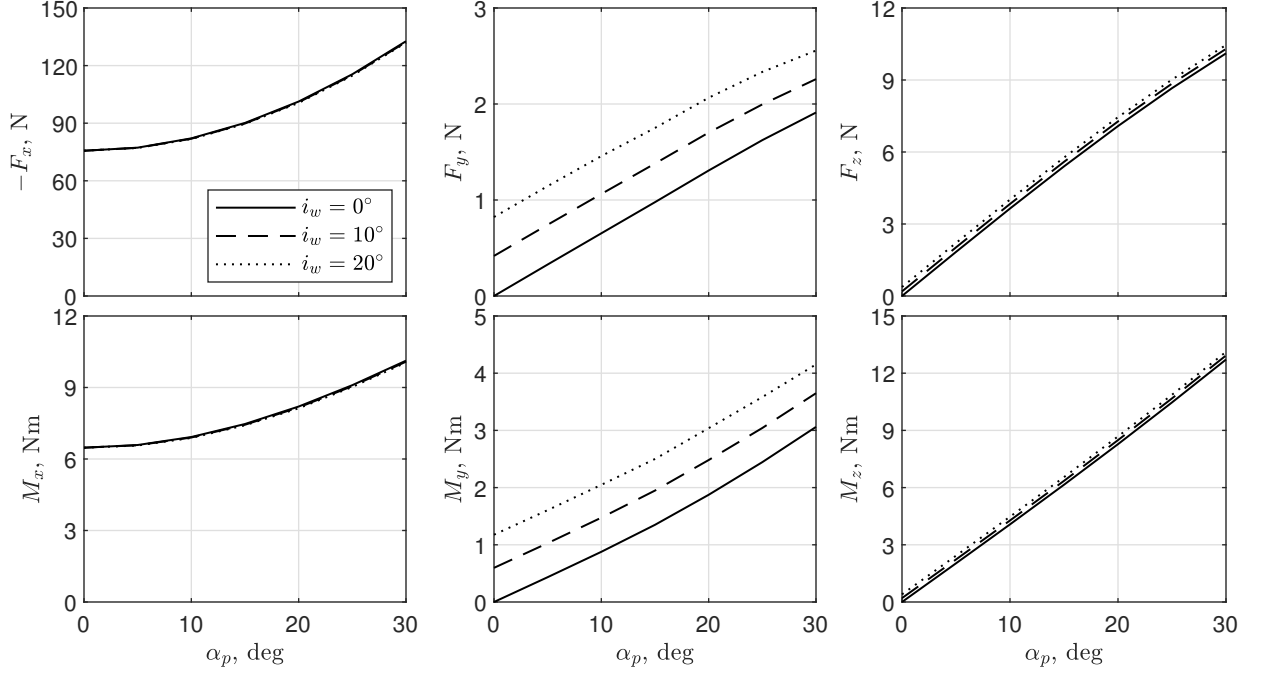


Figure 5.6: Comparison of propeller forces and moments over a sweep of α_p with varying α_w .

and 5.9 shows the decomposition of the axial induced velocity into contributions from the propeller (and its wake) and the wing (and its wake), respectively. Compared to the propeller's self-induced axial velocity, which is actually slightly less on the downwind side, the wing's contributions are more positive on the downwind side and are clearly responsible for the increase in pitching moment observed in Figure 5.6. The contours of axial induced velocity in Figure 5.9 also accurately reflect what was theorized in Figure 2.6. These results support our hypothesis that the wing's circulation (when located behind the propeller) is responsible for an induced velocity asymmetry across the propeller disk that adds to its propeller pitching moment.

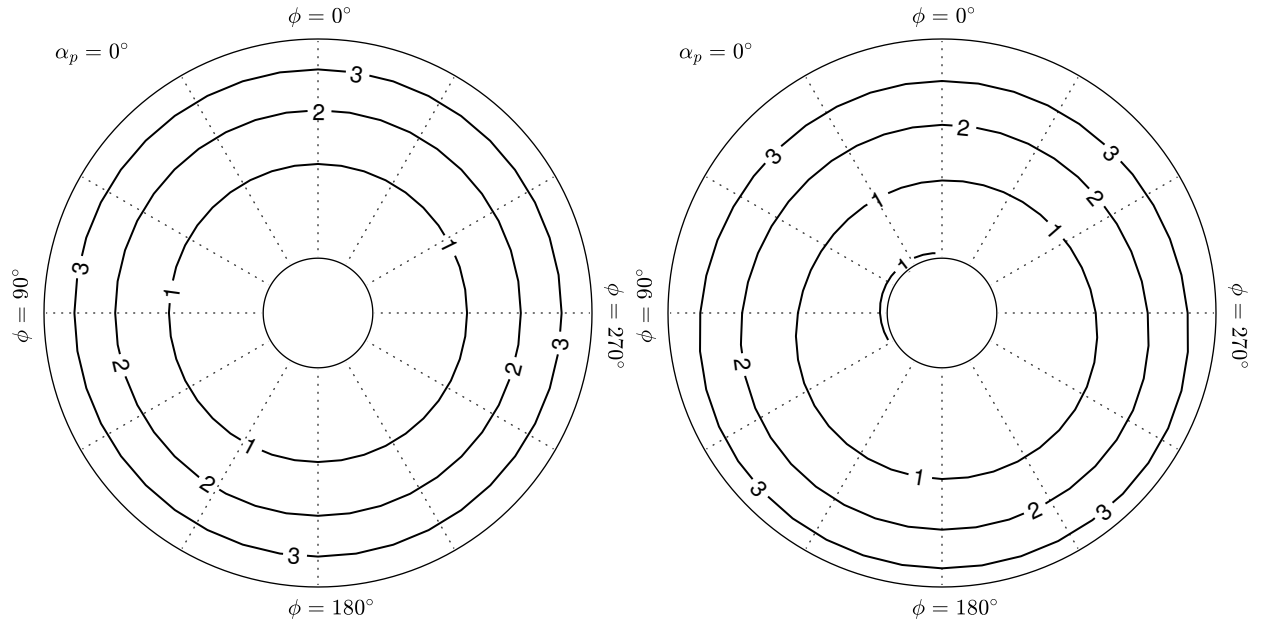


Figure 5.7: Contours of total axial induced velocity observed by the blades over the last revolution at $\alpha_p = 0^\circ$. $i_w = 0^\circ$ (left) and $i_w = 20^\circ$ (right).

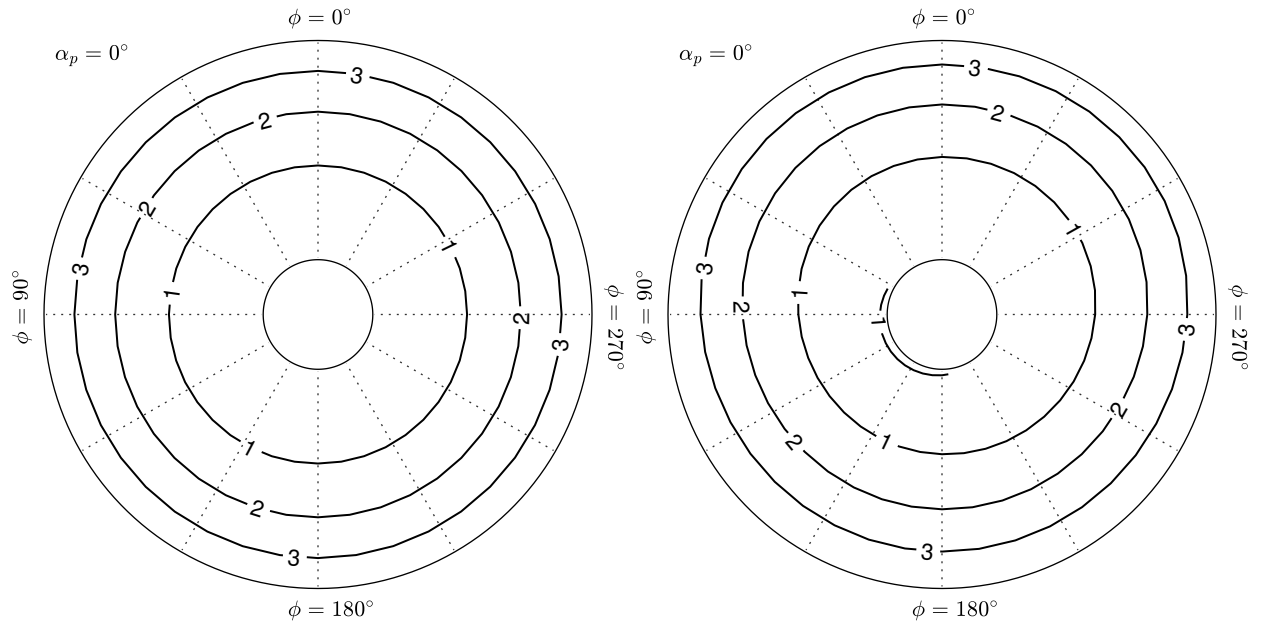


Figure 5.8: Contours of the propeller's bound and wake vortex rings' contribution to axial induced velocity observed by the blades at $\alpha_p = 0^\circ$. $i_w = 0^\circ$ (left) and $i_w = 20^\circ$ (right).

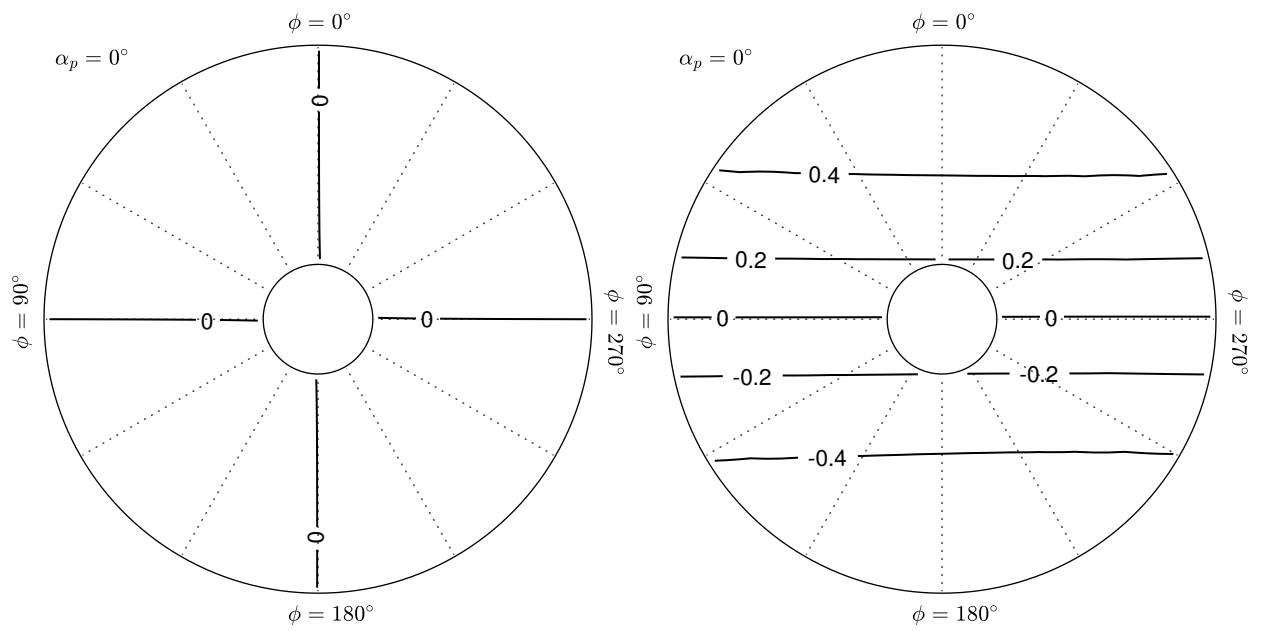


Figure 5.9: Contours of the wing's bound and wake vortex rings' contribution to axial induced velocity observed by the blades at $\alpha_p = 0^\circ$. $i_w = 0^\circ$ (left) and $i_w = 20^\circ$ (right).

CHAPTER 6

INVESTIGATING THE CONDITIONS FOR SIGNIFICANCE

It is evident from aviation history that propeller pitching moment was not a defining constraint in the stability and control of conventional takeoff and landing aircraft. The relatively low angles of attack and high flight speeds of CTOL aircraft would result in insignificant magnitudes of propeller pitching moment relative to the aircraft's control authority. However, observations from previous VTOL aircraft suggest that the low flight speeds and high angles of attack encountered by propellers during transition invalidate the assumptions of insignificance.

In this chapter, we use RoBIN to explore the conditions under which propeller pitching moment becomes significant for aircraft. First, we explore the characteristic trends of propeller pitching moment by generating performance maps over ranges of transition operational parameters. Then, we derive a generalizable metric of significance using the generated maps and a series of justifiable simplifying assumptions. Lastly, we vary certain VTOL design parameters to see their effects on the significance of propeller pitching moment. The studies will be limited to isolated propellers because the inviscid nature of RoBIN's analysis precludes accurate solutions of propeller and wing configurations at high angles of attack where the wing is fully stalled. However, given the revelations from the previous chapters on the effect of wing circulation, these results will still serve a useful purpose as a conservative lower bound for aircraft that have (upstream) propeller-wing interaction.

6.1 Pitching Moment Trends during Transition

Instead of using dimensional metrics, as has been the case thus far, the results presented here are in terms of nondimensional coefficients so that they may be generalized to pro-

propellers and aircraft of varying scale. Two types of coefficients are used: the “plain” coefficients (e.g., C_{Fx}) are normalized by tip dynamic pressure, whereas the coefficients with an infinity superscript (e.g., C_{Fx}^∞) are normalized by freestream dynamic pressure. The general forms of the force and moment coefficients are

$$C_F = \frac{F}{\rho_\infty n^2 D_p^4} \quad (6.1)$$

$$C_M = \frac{M}{\rho_\infty n^2 D_p^5} \quad (6.2)$$

$$C_F^\infty = \frac{F}{\frac{1}{2} \rho_\infty V_\infty^2 A_p} \quad (6.3)$$

$$C_M^\infty = \frac{M}{\frac{1}{2} \rho_\infty V_\infty^2 A_p D_p} \quad (6.4)$$

where n is the rotation speed in rev/s, A_p is the propeller area, and D_p is the propeller diameter. A useful property of these nondimensional coefficients is that, in the context of inviscid analysis, they are constant for a given propeller geometry at a given advance ratio and angle of attack, regardless of dimensional rotation speed, freestream velocity, or diameter via geometric scaling. Appendix A demonstrates this property.

Figure 6.1 shows a map of C_{My} divided by $-C_{Fx}$ over J and α_p . $C_{My}/-C_{Fx}$ reduces down to $M_y/(-F_x \times D_p)$, which is the percentage of the diameter by which the thrust vector must be translated down from the rotation axis to produce a moment about the origin equal to the propeller pitching moment. The sharp rise in $C_{My}/-C_{Fx}$ in the $\alpha_p = 0^\circ$ and $J = 0.6$ corner is where the propeller rotates too slowly and thrust coefficient goes to zero in the denominator. At $J < 0.3$, $C_{My}/-C_{Fx}$ generally tends to increase with J due to the wake becoming more skewed away from the rotation axis. Since the skewed wake causes the induced velocity asymmetry over the propeller disk, larger skew angles result in larger pitching moments. However, $C_{My}/-C_{Fx}$ does not necessarily continue to increase with J . At higher α_p where the propeller maintains positive thrust at $J > 0.3$, $C_{My}/-C_{Fx}$ is seen

to decrease as J increases. This is because the wake skew is limited by and asymptotes toward the freestream direction, and the diminishing increases in skew is counteracted by the wake stretching further over a single revolution at higher J . Since vortex velocity influence has an inverse-squared relationship with distance, the difference in the velocity influence magnitude at any two points on the propeller disk diminishes as the influencing vortex becomes further removed. Figure 6.2 visualizes the wakes of several $\alpha_p = 90^\circ$ propellers at varying J to demonstrate the stretching and asymptotic skewing of the wake.

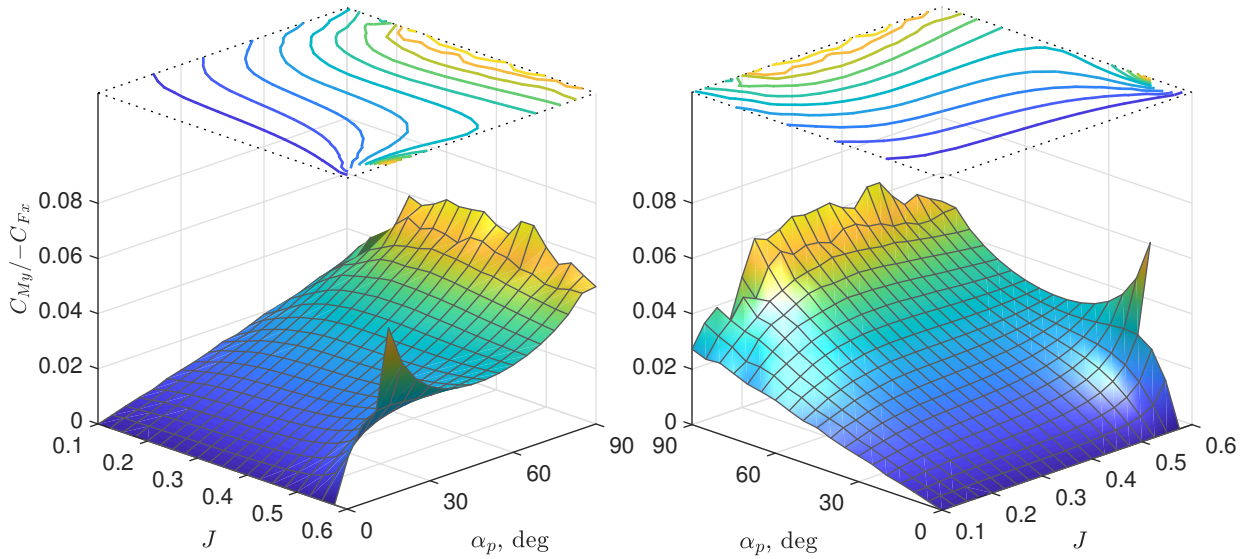


Figure 6.1: Surface of $C_{My}/-C_{Fx}$ over advance ratio and angle of attack.

Although $C_{My}/-C_{Fx}$ is useful for understanding how propeller pitching moment trends with different operating conditions, it is not necessarily representative of the propeller pitching moment's significance to aircraft. Many modern VTOL aircraft concepts can achieve trim via passive control surfaces or via differential thrust over distributed propulsors. If the propeller pitching moment were to be trimmed by an unblown horizontal stabilizer, whose control authority would be proportional to the freestream dynamic pressure, C_{My}^∞ would be the appropriate metric for comparison. Figure 6.3 shows the surface of C_{My}^∞ over J and α_p , where C_{My}^∞ rises rapidly as J decreases and α_p increases. The trend would likely continue to an extent as J decreased further, though it is unclear whether C_{My}^∞ would

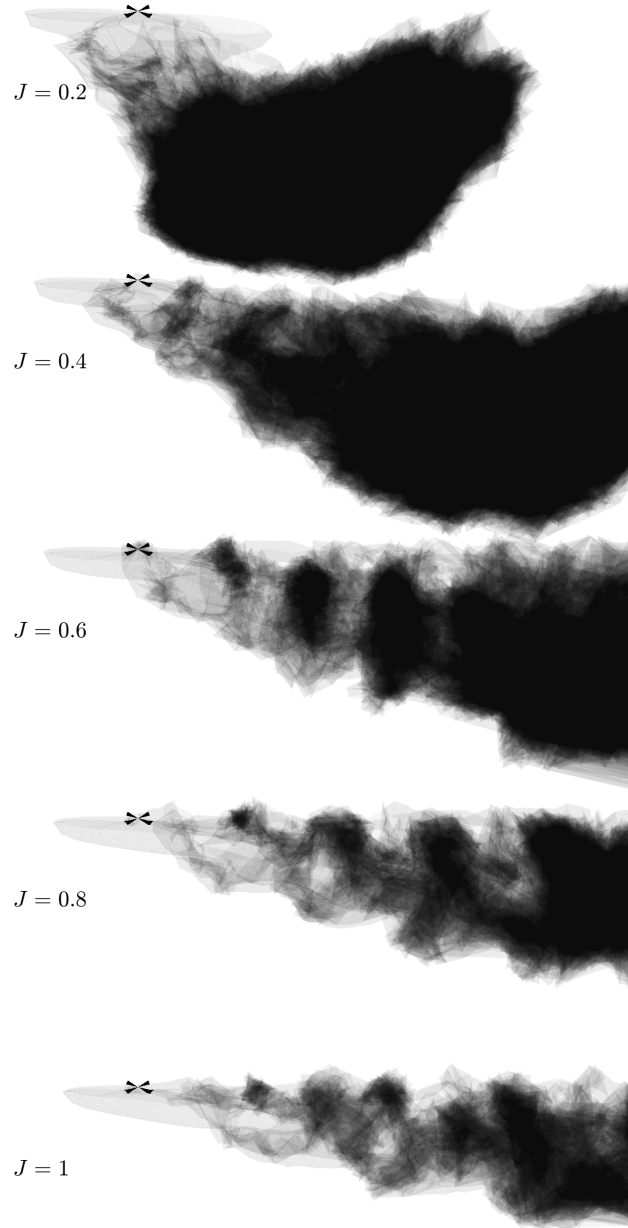


Figure 6.2: Wake visualization at a selection of advance ratios. $\alpha_p = 90^\circ$, $N_{rev} = 8$, freestream direction left to right.

ultimately resolve at zero or infinity at the indeterminate condition of $J = 0$. Figure 6.3 also provides more evidence as to why propeller pitching moment had not received much attention in the literature; C_{My}^∞ is very low in the $\alpha_p \leq 20^\circ$ region where propellers on conventional aircraft typically operate.

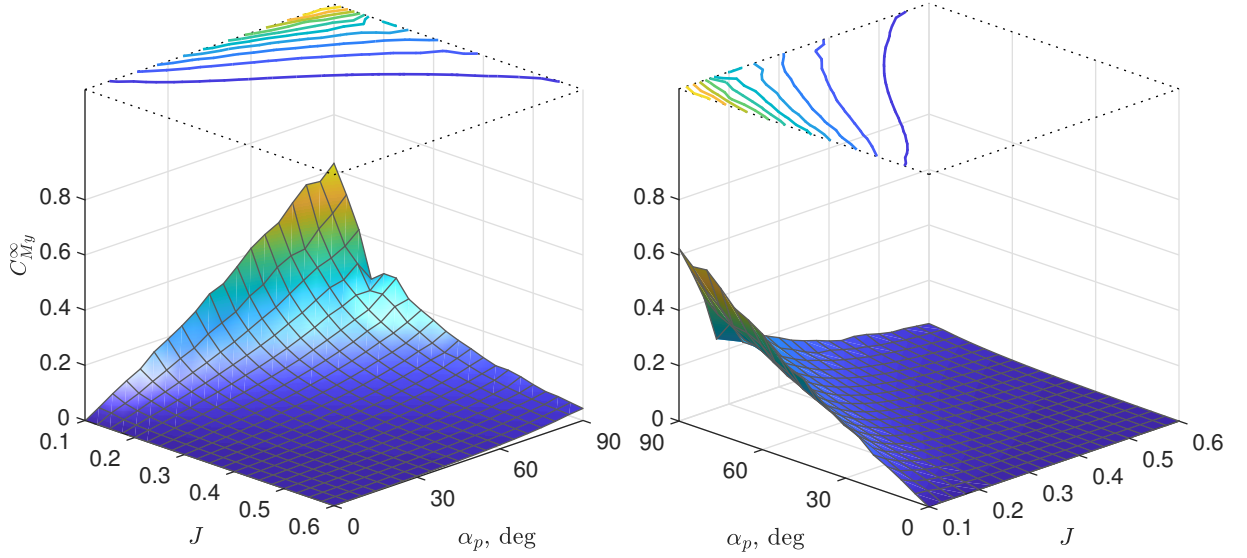


Figure 6.3: Surface of C_{My}^∞ over advance ratio and angle of attack.

If, instead, the pitching moment were to be trimmed by differential thrust (via another identical propeller), then the appropriate metric would be similar to $C_{My}/-C_{Fx}$, shown in Figure 6.1, except with the D_p reference length in the denominator replaced by the moment arm of the trimming propeller relative to the aircraft center of gravity. Unlike C_{My}^∞ , the $C_{My}/-C_{Fx}$ surface does not peak at near-zero J because the control authority of a propeller does not go to zero at static conditions.

6.2 A Generalizable Metric for Significance

To provide generalizable insight into the significance of propeller pitching moment, the following section describes the development of a metric that expresses propeller pitching moment as an effective displacement of the center of gravity in percent chord of the main wing.

Consider a tiltrotor-like VTOL aircraft with N_p identical propellers of area A_p that tilt through a range of α_p to transition between hover and cruise. In hover, it is assumed that the entire aircraft's weight, W , is distributed evenly amongst the propellers such that the disk loading in hover is $p_{DL} = \frac{W}{N_p A_p}$. Similarly, in cruise, it is assumed that W is fully supported

by the lift of a main wing of area S_w so that the wing loading in cruise is $p_{WL} = \frac{W}{S_w}$. For simplicity, the propellers' thrust, $-F_x = -C_{Fx}^\infty q_\infty A_p$, is assumed to be the only propeller force, and the main wing's lift, $L = C_L q_\infty S_w$, at any point is assumed to be generated at a constant lift coefficient. Lastly, we assume a rectangular wing with with aspect ratio \mathcal{R} so that the final expression can be represented in units of percent chord.

Given values of N_p , p_{DL} , p_{WL} , C_L , and \mathcal{R} , start by satisfying the vertical force balance for a level transition,

$$W = -C_{Fx}^\infty q_\infty A_p N_p \sin \alpha_p + C_L q_\infty S_w \quad (6.5)$$

Solving for the $-C_{Fx}^\infty$ required at a specific q_∞ and α_p gives

$$-C_{Fx}^\infty = \frac{W - C_L q_\infty S_w}{q_\infty N_p A_p \sin \alpha_p} = \frac{p_{DL} - \frac{C_L q_\infty p_{DL}}{p_{WL}}}{q_\infty \sin \alpha_p} \quad (6.6)$$

Then, use the data in Figure 6.4 to interpolate for the J that satisfies $-C_{Fx}^\infty$ at the specified α_p .

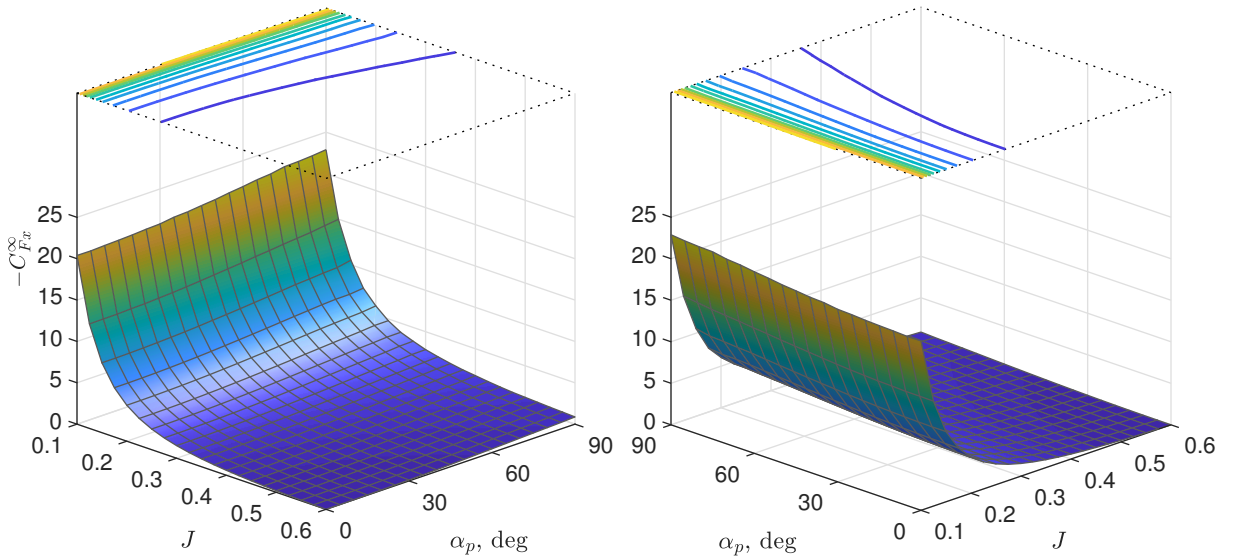


Figure 6.4: Surface of $-C_{Fx}^\infty$ over advance ratio and angle of attack.

The interpolated J and α_p are then referenced using the data in Figure 6.3 to find the C_{My}^∞

that would be produced by each propeller. Since

$$C_{My}^{\infty} = \frac{M_y}{q_{\infty} A_p D_p} \quad (6.7)$$

solve for M_y and express D_p in terms of A_p ,

$$M_y = C_{My}^{\infty} q_{\infty} A_p 2\sqrt{A_p/\pi} \quad (6.8)$$

Lastly, multiply both sides by N_p/W_c and manipulate the right-hand side into expressions of known values to get

$$\frac{N_p M_y}{W_c} = \frac{2C_{My}^{\infty} q_{\infty} \sqrt{A_p/\pi}}{p_{DL} c} = 2C_{My}^{\infty} q_{\infty} \sqrt{\frac{\mathcal{R} p_{WL}}{\pi N_p p_{DL}^3}} \quad (6.9)$$

The metric $\frac{N_p M_y}{W_c}$ is the total propeller pitching moment expressed in units of aircraft weight times wing chord, and because propeller-wing interaction was ignored, the metric as presented would be a conservative estimate in most cases. To demonstrate, Figure 6.5 shows the surface of $\frac{N_p M_y}{W_c}$ for an aircraft that uses the generic propeller with $N_p = 6$, $p_{DL} = 5$ lb/ft², $p_{WL} = 15$ lb/ft², $C_L = 0.65$, and $\mathcal{R} = 5$. The peak of roughly 0.1 means that the aircraft center of gravity is effectively shifted ten percent chord aft compared to if the propellers' thrust vectors were assumed to be centered at their hubs. However, an actual transition profile for a tiltrotor is unlikely to pass through the point $\alpha_p = 90^\circ$, $V_{\infty} = 40$ m/s, and a more realistic peak would be around eight percent for this aircraft.

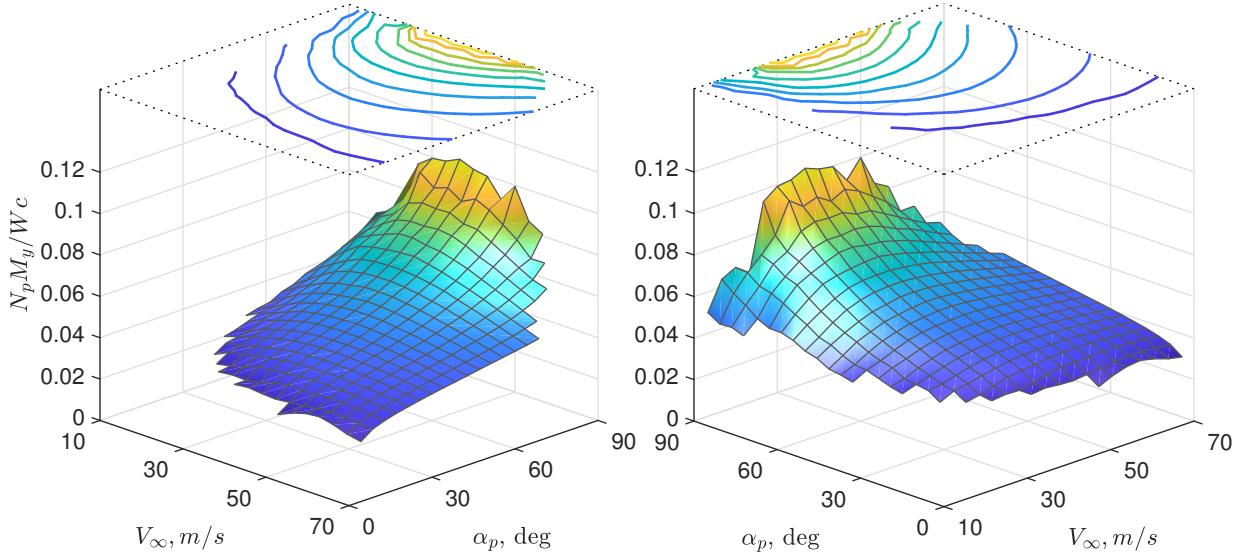


Figure 6.5: Example surface of $N_p M_y / W c$ over freestream velocity and angle of attack.

6.3 The Effect of Design Parameters on the Significance of Propeller Pitching Moment

A common trade-off considered during the design of VTOL aircraft is whether to have fewer, larger propellers or more, smaller propellers. Most aircraft from the previous VTOL era had only two or four lifting propellers because internal combustion engines were heavy and scaled unfavorably to smaller sizes. In contrast, most modern concepts take advantage of relatively scale-invariant electric motors to incorporate six or eight lifting propellers for better redundancy. The final decision on the number and size of the propellers is a far more involved decision that must consider aspects of cost, complexity, acoustics, and interactions with other components, but with the development of the metric of significance, we can at least provide some intuition on when propeller pitching moment may become an important consideration as well. To do this, we use the aircraft parameters that generated Figure 6.5 as a baseline and then perturb one parameter at a time by either halving or doubling it.

Figures 6.6 and 6.7 show the surfaces of $\frac{N_p M_y}{W c}$ for $N_p = 3$ and $N_p = 12$, respectively, disregarding the atypical odd number of propellers. Changing N_p while holding p_{DL} constant only changes the area of each propeller while holding total propeller area constant.

The area of each propeller varies inversely with N_p , but the radius of each propeller varies with the root inverse of N_p . Since the moment arm about the propeller origin for any thrust asymmetry scales proportionally with propeller radius, $\frac{N_p M_y}{W_c}$ scales by a factor of $\sqrt{2}$ when N_p halves and scales by a factor of $\frac{1}{\sqrt{2}}$ when N_p doubles. The overall shape of the surface does not change as indicated by the identical contours.

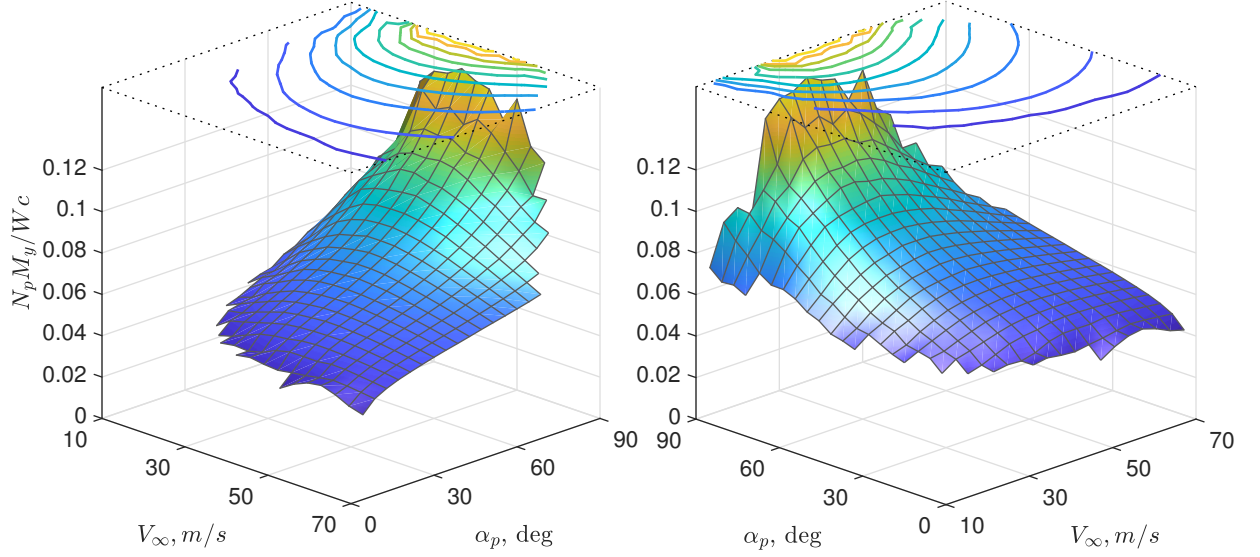


Figure 6.6: Surface of $N_p M_y / W_c$ with $N_p = 3$.

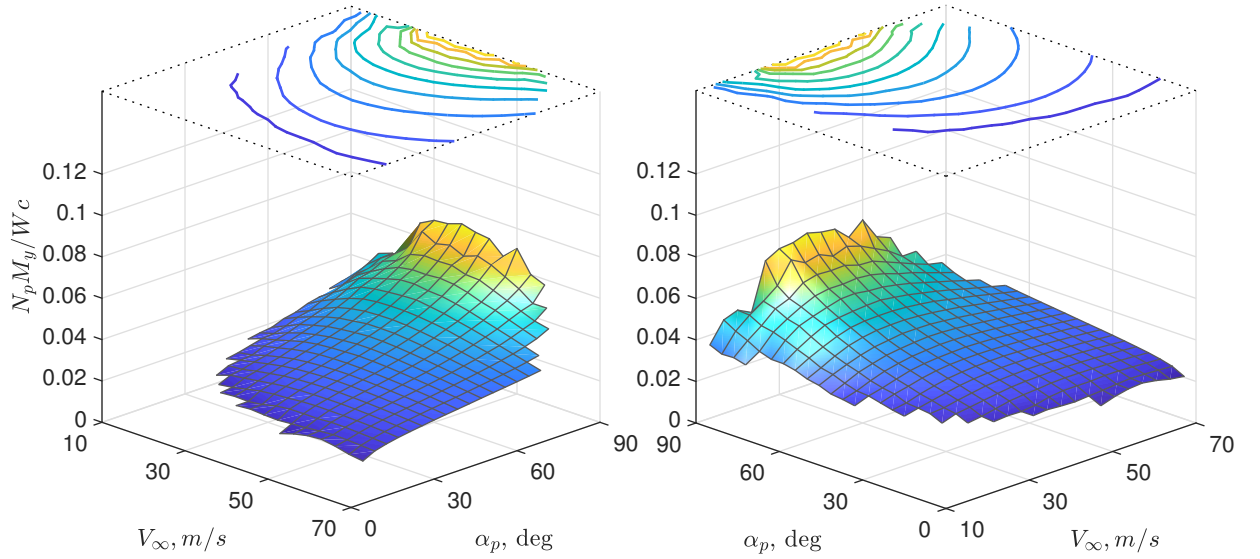


Figure 6.7: Surface of $N_p M_y / W_c$ with $N_p = 12$.

Figures 6.8 and 6.9 show the surfaces of $\frac{N_p M_y}{W_c}$ for $p_{DL} = 2.5 \text{ lb/ft}^2$ and $p_{DL} = 10 \text{ lb/ft}^2$, respectively. Similar to N_p , p_{DL} has an inverse relationship with propeller area, but with N_p held constant, each propeller must now vary thrust proportionally with the change in p_{DL} . The change in area has a similar effect as before— $\frac{N_p M_y}{W_c}$ scales by a factor of $\sqrt{2}$ when p_{DL} halves and scales by a factor of $\frac{1}{\sqrt{2}}$ when p_{DL} doubles. However, the change in propeller thrust now affects the resistance of the slipstream to skewing. With p_{DL} and thrust per propeller halved, a lower freestream velocity is required to achieve a given skew angle so the entire surface contracts along the V_∞ axis. The peak $\frac{N_p M_y}{W_c}$ is higher (due to the larger moment arm) and occurs earlier in transition at lower V_∞ but quickly drops as the wake asymptotes towards the freestream direction and stretches out. Conversely, with p_{DL} and thrust per propeller doubled, a higher freestream velocity is required to achieve a given skew angle so the entire surface expands along the V_∞ axis. The peak $\frac{N_p M_y}{W_c}$ is lower and occurs at higher V_∞ , but the higher momentum slipstream retains its asymmetric influence for a broader range of V_∞ .

Although not directly related to the trade-off in number and size of propellers, C_L and p_{WL} also affect the surface of $\frac{N_p M_y}{W_c}$ and are examined next. \mathcal{R} will not be examined because it was only included to allow the wing chord to be used as a reference length and has no meaningful effect on $\frac{N_p M_y}{W_c}$.

Figures 6.10 and 6.11 show the surfaces of $\frac{N_p M_y}{W_c}$ for $C_L = 0.325$ and $C_L = 1.3$, respectively. By holding p_{WL} constant, the total wing area cannot change so the aircraft must achieve a wing-lift-only cruise velocity that varies inversely with C_L . At any point in transition prior to cruise, the wing lift also varies proportionally with C_L so the propeller thrust must vary inversely with C_L to maintain level transition. In the case that C_L is halved, the propellers must produce more thrust, resulting in a higher momentum wake that resists skewing. If C_L is doubled, the propellers produce less thrust, and the wake is less resistant to skewing. Since the wing's contribution to lift is very small at low V_∞ , the surfaces of $\frac{N_p M_y}{W_c}$ are nearly identical to that of the baseline, regardless of C_L . However, at higher V_∞ ,

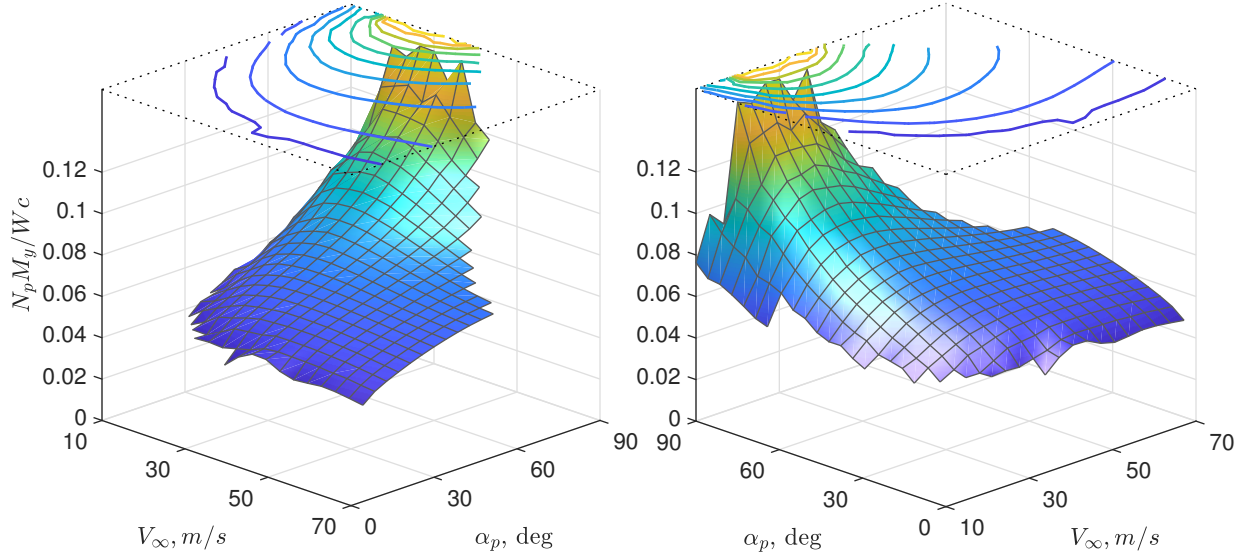


Figure 6.8: Surface of $N_p M_y / Wc$ with $p_{DL} = 2.5 \text{ lb/ft}^2$.

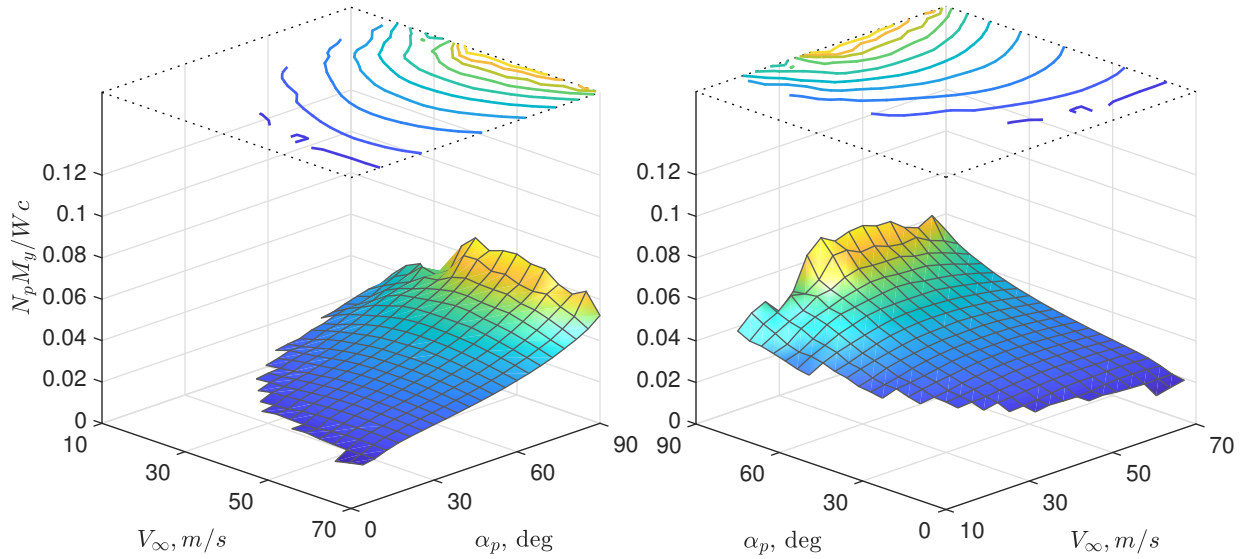


Figure 6.9: Surface of $N_p M_y / Wc$ with $p_{DL} = 10 \text{ lb/ft}^2$.

the surface broadens or narrows in a manner similar to that seen in Figures 6.9 and 6.8, respectively. Note that the peak $\frac{N_p M_y}{Wc}$ varies much less when compared to the figures of the other design parameters.

Figures 6.12 and 6.13 show the surfaces of $\frac{N_p M_y}{Wc}$ for $p_{WL} = 7.5 \text{ lb/ft}^2$ and $p_{WL} = 30 \text{ lb/ft}^2$, respectively. Varying p_{WL} has the same effect on wing lift as varying C_L inversely,

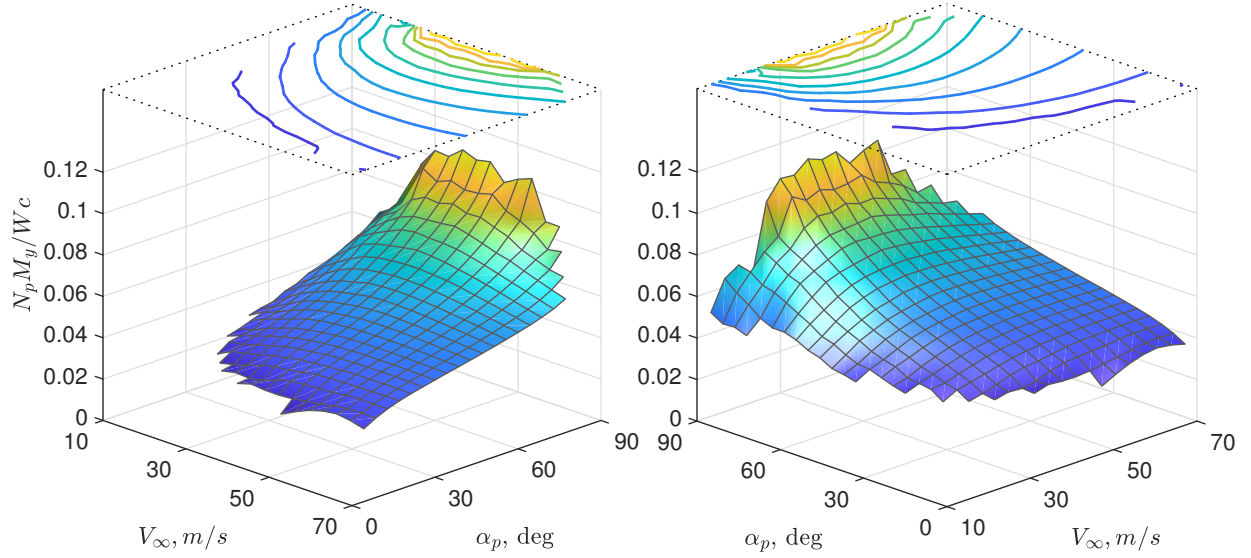


Figure 6.10: Surface of $N_p M_y / W c$ with $C_L = 0.325$.

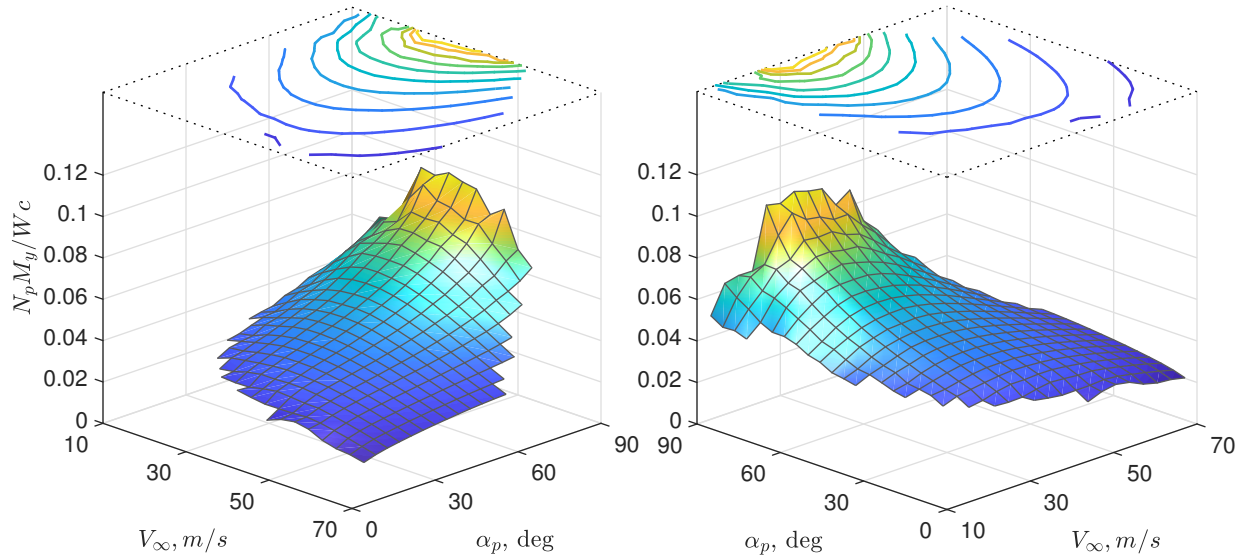


Figure 6.11: Surface of $N_p M_y / W c$ with $C_L = 1.3$.

except that the wing lift is changed due to wing area instead of C_L . Thus, the effect of p_{WL} on total pitching moment should be identical (but inverted) to that of C_L . This is confirmed by the identical contours seen between Figures 6.11 and 6.12 and between Figures 6.10 and 6.13. However, because the wing area changes with p_{WL} while \mathcal{A} remains constant, the chord length also changes and exaggerates the effect of p_{WL} on the chord-normalized

metric of significance.

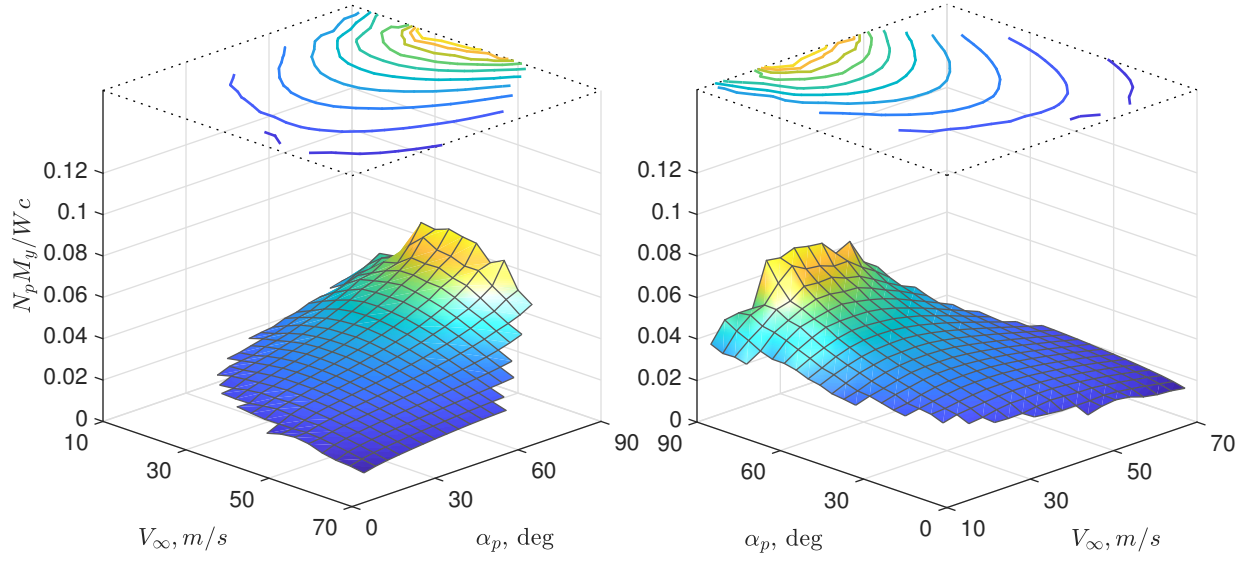


Figure 6.12: Surface of $N_p M_y / W c$ with $p_{WL} = 7.5 \text{ lb/ft}^2$.

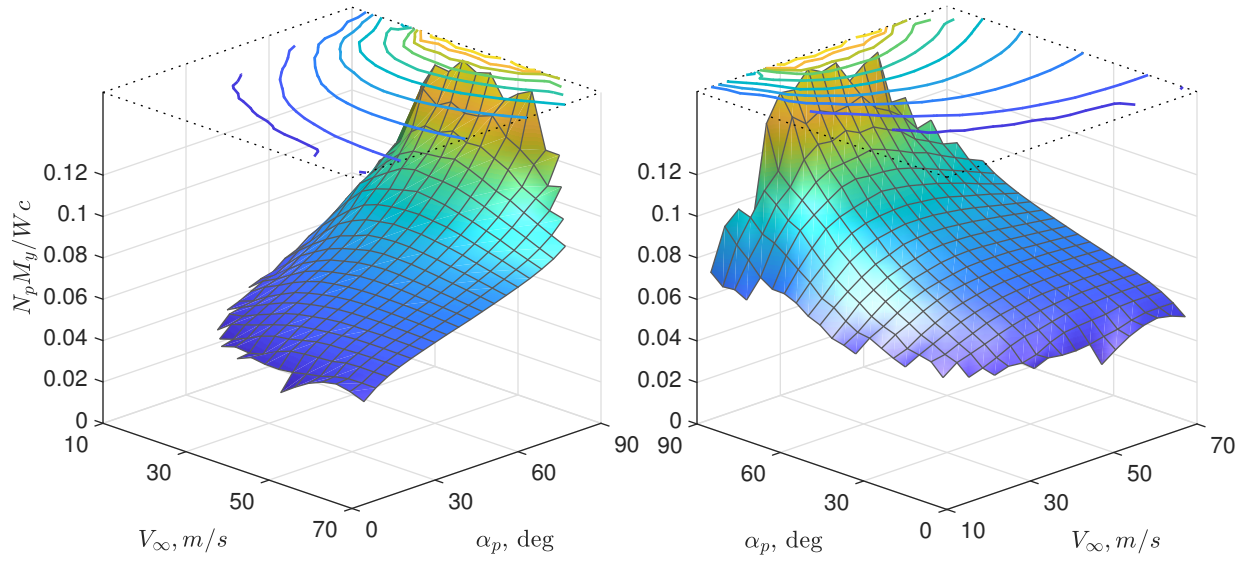


Figure 6.13: Surface of $N_p M_y / W c$ with $p_{WL} = 30 \text{ lb/ft}^2$.

CHAPTER 7

CONCLUSION AND RECOMMENDATIONS

In this dissertation, we have shown that propellers operating at an angle of attack experience a pitching moment about their hub that is primarily caused by an asymmetry in the axial induced velocity distribution over the disk about the pitch axis. The effect is present for isolated propellers, but interactions with other components can further increase the pitching moment. In the case of an isolated propeller, the wake skews in the freestream direction, resulting in reduced induced velocity on and increased thrust from the upwind half of the propeller. In the case of a propeller positioned upstream of a lifting wing, the wing's circulation similarly reduces the induced velocity on the upwind half while also increasing the induced velocity on the downwind half of the propeller.

7.1 Impacts on Aircraft Design

Compared to the shaft torque and yawing moment, propeller pitching moment is the weakest of the propeller moments. However, the magnitudes can still be considerable at low advance ratios and high angles of attack where VTOL aircraft must operate to transition between hover and forward flight. A conservative estimate using generic geometries puts the peak total propeller pitching moment on the order of an effective displacement of the aircraft center of gravity by several percent of the wing chord. The magnitude of the peak pitching moment was found to depend strongly on the design of the propulsion system. All else being equal, having fewer, larger propellers produced more significant total propeller pitching moments than having more, smaller propellers. Reducing the propeller diameter, whether by increasing disk loading or by increasing the number of propellers, generally reduced the peak total pitching moment by a factor proportional to the reduction in diameter. Increasing disk loading had the additional effect of delaying and broadening the range of

transition velocities over which propeller pitching moment was most significant because the higher momentum wake resisted skewing toward the freestream direction. These trends explain why the previous generation of VTOL aircraft, which were limited by internal combustion engine technology to fewer, larger propellers tended to have more difficulty with longitudinal stability and control in transition. Fortunately, with the advent of distributed electric propulsion, modern VTOLs have more freedom to use smaller propellers and avoid the most extreme propeller pitching moments.

If the reader is wondering whether or not one needs to account for propeller pitching moment early in the design process, the answer is likely dependent on the vehicle design and expected trimming solution. If the vehicle will have a balanced longitudinal distribution of propellers operating throughout transition and is expected to trim via a thrust differential between fore and aft propellers, then an early and accurate account of propeller pitching moment is probably not critical. The propeller thrusts need only be redistributed by a few percent if the propellers have moment arms on the order of one diameter or more from the aircraft center of gravity. In contrast, if the aircraft has a disproportionate number of propellers concentrated at one longitudinal position, then designing for propeller pitching moment early will be more critical. For example, during the previous VTOL era, later aircraft designs converged toward a hybrid tiltwing-deflected slipstream approach whereby a large-chord flap was integrated on a single blown tilting wing [114–117]. The flap, which generated a large negative pitching moment, would be programmed with a deflection schedule throughout transition to counteract the positive propeller pitching moment. Vehicles such as the Canadair CL-84 [118] and retrofitted VZ-2 [119] successfully demonstrated this approach but required extensive ground and flight testing to determine the proper deflection schedule.

Aside from trimming away the propeller pitching moment, another approach would be to reduce the impact of any propeller pitching moment by using any tilting actuation associated with transition to naturally displace the aircraft center of gravity or propeller

thrust axis by the distance necessary to counteract the pitching moment. While elegant, this type of solution is likely the most dependent on an early and accurate prediction of longitudinal stability characteristics since any errors would likely require the repositioning of major components to achieve trim. Surprisingly, the use of non-rigidly attached propeller blades may not be a solution to reducing propeller pitching moment. A study comparing rigid and flapping propellers on the VZ-2 [5] found the flapping blades to induce a larger nose-up pitching moment on the aircraft.

7.2 Recommendations for Future Work

The work presented here was focused on the quasi-steady loads of a rigid propeller which, although convenient for analysis, is a limited view of a simplified problem. For real world applications, the unsteady loading of propellers at angles of attack can have greater ramifications such as inducing aeroelastic instabilities or accelerating material fatigue. The simplified geometry representation used in VLMs like RoBIN presents an opportunity to couple unsteady aerodynamics with low-order structural modeling for early-design aeroelastic analyses, if desired.

Another area of work is the improvement of the aerodynamic modeling. The X-57 HLP validation results showed that the reduction in induced velocity can cause blades to stall, an effect which cannot be directly modeled with inviscid methods. One could potentially estimate the local angle of attack in the VLM and include viscous effects by substituting forces found via a table look-up of viscous 2D airfoil data or by adding a correction term to the inviscid forces calculated within the VLM. Comparisons of the thrust distributions in Chapter 4 had also suggested that the inviscid results could be improved by allowing the wake shedding location to change dynamically as determined by the local flow direction along the surface perimeter.

Appendices

APPENDIX A

CONSTANCY OF AERODYNAMIC COEFFICIENTS WITH ADVANCE RATIO

In the context of an inviscid solution, aerodynamic coefficients are constant for a given advance ratio regardless of the dimensional freestream velocity, rotation speed, and propeller diameter. Figures A.1 and A.2 show the thrust and pitching moment coefficients, respectively, of a generic propeller operated at $\alpha_p = 60^\circ$ over a range of advance ratios. Each plot contains nine curves for each coefficient, with each curve representing the same advance ratio sweep achieved by appropriately varying the rotation speed for three different freestream velocities and with the propeller geometrically scaled to three different diameters. The curves are largely identical with the measurements fanning out gradually at the lower advance ratios. The fanning out is due to the chaotic nature of the wake propagation in high loading conditions; slight differences in velocity influence due to numerical imprecision propagate over time, resulting in wake structure differences significant enough to affect the induced velocity distribution at the disk. The coefficient variations seem to be random in nature, inferred by the intersection of curves between different advance ratios, and can be considered noise in the data. The noise is more pronounced in the pitching moment coefficients than the thrust coefficients because the wake structure discrepancies primarily affect the *distribution* of induced velocity at the disk rather than the average. Based on this study, we limited the range of advance ratios examined to $J \geq 0.1$.

The simulation settings used were $N_{ppb} = 225$, $N_{tpr} = 60$, and $N_{rev} = 8$. If computation time were not an issue, the wake propagation noise could be reduced by increasing either the grid or timestep resolutions.

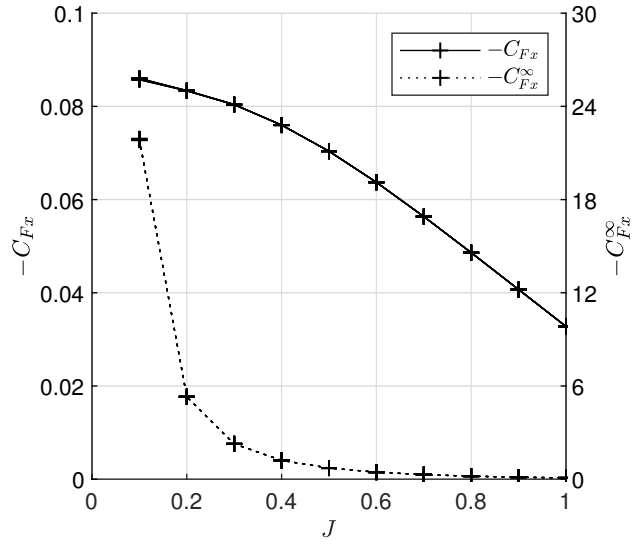


Figure A.1: Thrust coefficients versus advance ratio for generic propeller at $\alpha_p = 60^\circ$.

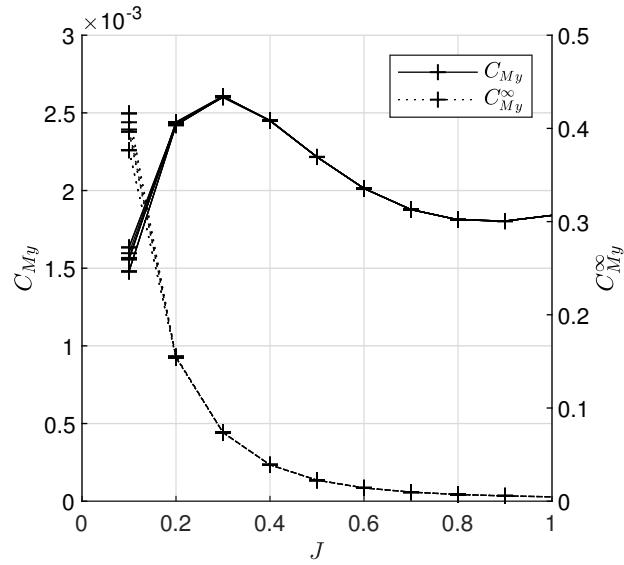


Figure A.2: Pitching moment coefficients versus advance ratio for generic propeller at $\alpha_p = 60^\circ$.

APPENDIX B

PROPELLER IN FORWARD FLIGHT VALIDATION

A basic axial forward flight test case was used as a supplemental validation of RoBIN. The X-57 HLP propeller geometry was used once again, and results were compared against those from XROTOR [120], a tool used throughout the design of the X-57 aircraft, and OVERFLOW. XROTOR is a commonly used low-order propeller analysis tool that models propeller blades as lifting lines and wakes as induced velocity influences calculated in one of three ways: 1) the graded momentum formulation, which uses the Betz-Prandtl tip loss fudge factor, 2) the potential formulation, which extends Goldstein's induced velocity model for helical wakes to all blade numbers, and 3) the vortex formulation, which calculates the induced velocity from discrete vortices placed along a rigid helicoidal wake surface. The graded momentum formulation is only valid for advance ratios less than about 0.5 or for high blade counts and so was omitted from comparison.

XROTOR calculates the lift and drag of a blade section by first calculating the angle of attack resulting from the kinematic motion and wake induced velocity model. A user-specified Reynolds-corrected quadratic drag polar is then used to produce the sectional lift and drag. If the angle of attack is outside of a user-specified linear region of the lift curve, a simple (but undocumented) pressure drag correction is added to account for stall. The drag polar model used in this XROTOR analysis was calibrated using viscous XFOIL predictions for the MH114 airfoil.

Figure B.1 compares thrust coefficient over a range of advance ratios. RoBIN's results are consistent with the thrust comparison seen in Figure 4.7. The overprediction in thrust at the design condition of $J = 0.68$ is seen to manifest as a near-constant thrust coefficient offset over the range of advance ratios. A constant offset such as this suggests a possible misrepresentation of the blade or wake geometry. For example, the camber line

representation in RoBIN may not be the best representation of the average location of the bound vorticity. Alternatively, the wake shedding angle, currently set to be aligned with the path of the trailing edge over the last time step, may be too steep or too shallow. Still, RoBIN's predictions are considerably better than those of XROTOR, which overpredict thrust coefficient by 20-25%.

Figure B.2 shows that RoBIN's power coefficient predictions are also more accurate than those of XROTOR. RoBIN's slight underprediction at the lower advance ratios was expected because RoBIN is an inviscid code and cannot capture profile power, but we are unsure why RoBIN slightly overpredicts power coefficient at higher advance ratios. A potential explanation may be that the OVERFLOW analyses included a nacelle, which would reduce the induced drag near the blade root. RoBIN's simulation settings were $N_{ppb} = 400$, $N_{tpv} = 60$, and $N_{rev} = 8$.

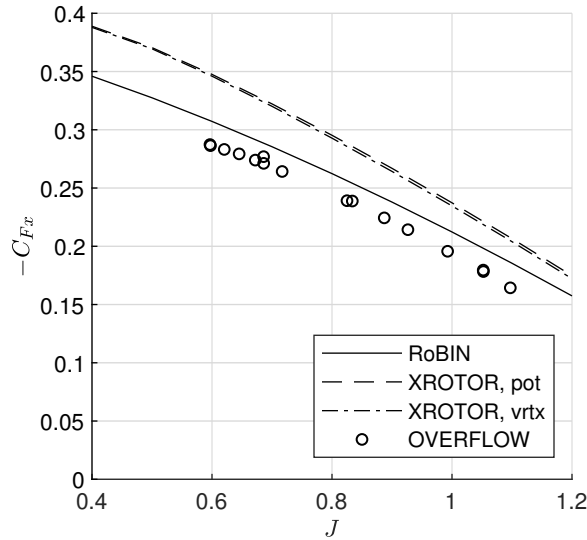


Figure B.1: Thrust coefficient vs advance ratio for isolated HLP.

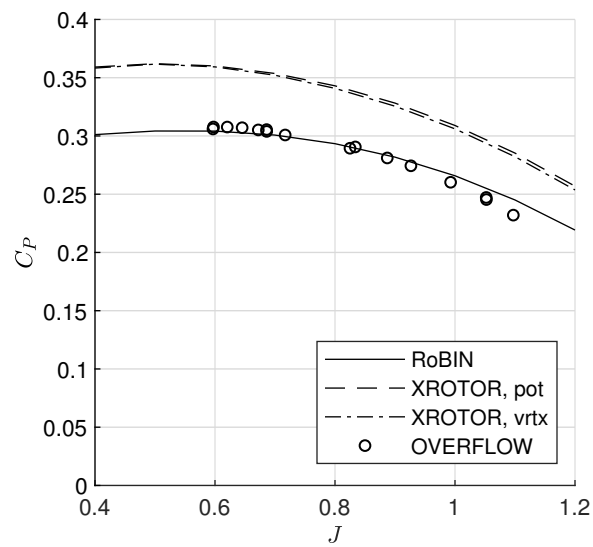


Figure B.2: Power coefficient vs advance ratio for isolated HLP.

REFERENCES

- [1] J. P. Reeder. "Handling Qualities Experience with Several VTOL Research Aircraft". In: *NASA Conference on V/STOL Aircraft*. 1960.
- [2] William A. Newsom Jr and Louis P. Tosti. *Force-Test Investigation of the Stability and Control Characteristics of a 1/4-Scale Model of a Tilt-Wing Vertical-Take-Off-and-Landing Aircraft*. Tech. rep. NASA-MEMO-11-3-58L. National Aeronautics and Space Administration, 1959.
- [3] Louis P. Tosti. *Flight investigation of the stability and control characteristics of a 1/4-scale model of a tilt-wing vertical-take-off-and-landing aircraft*. Tech. rep. NASA-MEMO-11-4-58L. National Aeronautics and Space Administration, 1959.
- [4] Louis P. Tosti. *Aerodynamic Characteristics of a 1/4-Scale Model of a Tilt-Wing VTOL Aircraft at High Angles of Wing Incidence*. Tech. rep. NASA-TN-D-390. National Aeronautics and Space Administration, 1960.
- [5] Louis P. Tosti. *Longitudinal Stability and Control of a Tilt-wing VTOL Aircraft Model with Rigid and Flapping Propeller Blades*. Tech. rep. NASA-TN-D-1365. National Aeronautics and Space Administration, 1962.
- [6] Robert J. Pegg. *Summary of Flight-test Results of the VZ-2 Tilt-wing Aircraft*. Tech. rep. NASA-TN-D-989. National Aeronautics and Space Administration, 1962.
- [7] Marvin P Fink. *Full-Scale Wind-Tunnel Investigation of the VZ-5 Four-Propeller Deflected-Slipstream VTOL Airplane*. Tech. rep. NASA-TM-SX-805. National Aeronautics and Space Administration, 1963.
- [8] Harry A James et al. *Wind-Tunnel and Piloted Flight Simulator Investigation of a Deflected-Slipstream VTOL Airplane, the Ryan VZ-3RY*. Tech. rep. NASA-TN-D-89. National Aeronautics and Space Administration, 1959.
- [9] Howard L Turner and Fred J Drinkwater III. *Longitudinal Trim Characteristics of a Deflected Slipstream V/STOL Aircraft During Level Flight at Transition Flight Speeds*. Tech. rep. NASA-TN-D-1430. National Aeronautics and Space Administration, 1962.
- [10] Howard L Turner and Fred J Drinkwater III. *Some Flight Characteristics of a Deflected Slipstream V/STOL Aircraft*. Tech. rep. NASA-TN-D-1891. National Aeronautics and Space Administration, 1963.
- [11] John W Draper and Richard E Kuhn. *Investigation of the Aerodynamic Characteristics of a Model Wing-Propeller Combination and of the Wing and Propeller*

Separately at Angles of Attack up to 90 Degrees. Tech. rep. NACA-TN-3304. National Advisory Committee for Aeronautics, 1954.

- [12] Richard E. Kuhn and John W. Draper. *An Investigation of a Wing-Propeller Configuration Employing Large-Chord Plain Flaps and Large-Diameter Propellers for Low-Speed Flight and Vertical Take-Off*. Tech. rep. NASA-TN-3307. National Advisory Committee for Aeronautics, 1954.
- [13] Herbert S Ribner. *Propellers in Yaw*. Tech. rep. NACA-TR-820. National Advisory Committee for Aeronautics, 1945.
- [14] W F Phillips, E A Anderson, and Q J Kelly. “Predicting the Contribution of Running Propellers to Aircraft Stability Derivatives”. In: *Journal of Aircraft* 40.6 (2003), pp. 1107–1114.
- [15] John De Young. “Propeller at High Incidence”. In: *Journal of Aircraft* 2.3 (1965), pp. 241–250.
- [16] O. Flachsbart and G. Krober. *Experimental Investigation of Aircraft Propellers Exposed to Oblique Air Currents*. Tech. rep. NACA-TM-562. National Advisory Committee for Aeronautics, 1930.
- [17] Everett Parker Lesley, George F Worley, and Stanley Moy. *Air Propellers in Yaw*. Tech. rep. NACA-TR-597. National Advisory Committee for Aeronautics, 1937.
- [18] Robert E Pendley. *Effect of Propeller-Axis Angle of Attack on Thrust Distribution over the Propeller Disk in Relation to Wake-Survey Measurement of Thrust*. Tech. rep. NACA-ARR-L5J02b. National Advisory Committee for Aeronautics, 1945.
- [19] H Clyde McLemore and Michael D Cannon. *Aerodynamic Investigation of a Four-blade Propeller Operating Through an Angle-of-Attack Range from 0 to 180 degrees*. Tech. rep. NACA-TN-3228. National Advisory Committee for Aeronautics, 1954.
- [20] Paul F Yaggy and Vernon L Rogallo. *A Wind-Tunnel Investigation of Three Propellers Through an Angle-of-attack Range from 0 to 85 degrees*. Tech. rep. NASA-TN-D-318. National Aeronautics and Space Administration, 1960.
- [21] Paul L Coe Jr, Garl L Gentry Jr, and Dana Morris Dunham. *Low-Speed Wind-Tunnel Tests of an Advanced Eight-Bladed Propeller*. Tech. rep. NASA-TM-86364. National Aeronautics and Space Administration, 1985.
- [22] Wilmer H Reed III and Samuel R Bland. *An Analytical Treatment of Aircraft Propeller Precession Instability*. Tech. rep. NASA-TN-D-659. National Aeronautics and Space Administration, 1961.

- [23] John C. Houbolt and III Wilmer H. Reed. “Propeller-Nacelle Whirl Flutter”. In: *Journal of the Aerospace Sciences* 29.3 (1962), pp. 333–346.
- [24] Samuel R Bland and Robert M Bennett. *Wind-tunnel Measurement of Propeller Whirl-Flutter Speeds and Static-Stability Derivatives and Comparison with Theory*. Tech. rep. NASA-TN-D-1807. National Aeronautics and Space Administration, 1963.
- [25] Harold Fluk. *The X-19 V/STOL technology: A critical review*. Tech. rep. AFFDL-TR-66-195. Air Force Flight Dynamics Laboratory, 1967.
- [26] Yuchen Leng et al. “Aerodynamic Modeling of Propeller Forces and Moments at High Angle of Incidence”. In: *AIAA Scitech 2019 Forum*. AIAA 2019-1332. 2019.
- [27] Bertrand Theys et al. “Experimental and Numerical Study of Micro-Aerial-Vehicle Propeller Performance in Oblique Flow”. In: *Journal of Aircraft* 54.3 (2017), pp. 1076–1084.
- [28] Matthew Misiorowski, Farhan Gandhi, and Phuriwat Anusonti-Inthra. “Computational Analysis of Rotor-Blown-Wing for eVTOL Applications”. In: *Vertical Flight Society 75th Annual Forum and Technology Display*. 2019.
- [29] Jan Gerhard Schepers. “Engineering Models in Wind Energy Aerodynamics: Development, Implementation and Analysis Using Dedicated Aerodynamic Measurements”. PhD thesis. TU Delft, 2012.
- [30] Robert Niemiec and Farhan Gandhi. “Effects of Inflow Model on Simulated Aeromechanics of a Quadrotor Helicopter”. In: *72nd Annual Forum of the American Helicopter Society International*. 2016.
- [31] Matthew Misiorowski, Farhan Gandhi, and Assad A Oberai. “Computational Study on Rotor Interactional Effects for a Quadcopter in Edgewise Flight”. In: *AIAA Journal* 57.12 (2019), pp. 5309–5319.
- [32] *Helicopter Flying Handbook*. FAA-H-8083-21B. United States Department of Transportation, Federal Aviation Administration, Airman Testing Branch, 2019.
- [33] Snorri Gudmundsson. *General Aviation Aircraft Design: Applied Methods and Procedures*. Butterworth-Heinemann, 2013.
- [34] William Amatt, William E Bates, and Henry V Borst. *Summary of Propeller Design Procedures and Data. Volume 2. Structural Analysis and Blade Design*. Tech. rep. AD-774-836. US Army Air Mobility Research and Development Laboratory, 1973.

- [35] AS Aljabri and AC Hughes. “Wind Tunnel Investigation of the Interaction of Propeller Slipstream with Nacelle/Wing/Flap Combinations”. In: *AGARD Aerodyn. and Acoustics of Propellers 10 p(SEE N 86-11147 02-01)* (1985).
- [36] Marc E Brenckmann. “Experimental Investigation of the Aerodynamics of a Wing in a Slipstream”. In: *Journal of the Aerospace Sciences* 25.5 (1958).
- [37] FM Catalano. “On the Effects of an Installed Propeller Slipstream on Wing Aerodynamic Characteristics”. In: *Acta Polytechnica* 44.3 (2004).
- [38] Kwanchai Chinwicharnam et al. “Aerodynamic Characteristics of a Low Aspect Ratio Wing and Propeller Interaction for a Tilt-Body MAV”. In: *International Journal of Micro Air Vehicles* 5.4 (2013).
- [39] Gilles Fratello, Daniel Favier, and Christian Maresca. “Experimental and Numerical Study of the Propeller/Fixed Wing Interaction”. In: *Journal of Aircraft* 28.6 (1991).
- [40] Brian J Gamble and Mark F Reeder. “Experimental Analysis of Propeller-Wing Interactions for a Micro Air Vehicle”. In: *Journal of aircraft* 46.1 (2009).
- [41] Garl L Gentry Jr, MA Takallu, and Zachary T Applin. *Aerodynamic Characteristics of a Propeller-Powered High-Lift Semispan Wing*. Tech. rep. TM 4541. National Aeronautics and Space Administration Langley Research Center, 1994.
- [42] Robert T Johnson, David P Witkowski, and John P Sullivan. *Experimental Results of a Propeller/Wing Interaction Study*. Tech. rep. 910998. SAE Technical Paper, 1991.
- [43] RA Maarsingh. *Evaluation of Ting’s Method for the Calculation of the Lift Distribution on a Wing in Propulsive Jets*. Tech. rep. NLR TR 80078 U. Nationaal Lucht-en Ruimtevaartlaboratorium, 1979.
- [44] L Prandtl. *Applications of Modern Hydrodynamics to Aeronautics*. Tech. rep. NACA-TR-116. National Advisory Committee for Aeronautics, 1921.
- [45] J Stuper. *Effect of Propeller Slipstream on Wing and Tail*. Tech. rep. TM 874. National Advisory Committee for Aeronautics, 1938.
- [46] LLM Veldhuis, S Nebiolo, and Polytechnico di Torino. “A Propeller Integration Study Comparing Experimental Data with Numerical Flow Solutions Based on the Navier-Stokes Equations”. In: *International Congress of Aeronautical Sciences, Harrogate, United Kingdom*. 2000.

- [47] LLM Veldhuis. “Review of Propeller-Wing Aerodynamic Interference”. In: *24th International Congress of the Aeronautical Sciences*. 2004.
- [48] Leonardus Louis Maria Veldhuis. “Propeller Wing Aerodynamic Interference”. PhD thesis. Delft University of Technology, 2005.
- [49] Dave P. Witkowski, Alex K. H. Lee, and John P. Sullivan. “Aerodynamic Interaction Between Propellers and Wings”. In: *Journal of Aircraft* 26.9 (1989), pp. 829–836.
- [50] T Zandbergen and RA Maarsingh. *Evaluation of Levinsky’s Method for the Calculation of the Lift Distribution on a Wing in Propulsive Jets*. Tech. rep. NLR TR 77104 U. Nationaal Lucht-en Ruimtevaartlaboratorium, 1979.
- [51] E Cumberbatch. *A Lifting Surface Theory for Wings at High Angles of Attack Extending Through Multiple Jets*. Tech. rep. Vehicle Research Corporation, 1963.
- [52] Jameson Antony. *Analysis of Wing Slipstream Flow Interaction*. Tech. rep. NASA-CR-1632. National Aeronautics and Space Administration, 1970.
- [53] ES Levinsky et al. “Lifting Surface Theory for V/STOL Aircraft in Transition and Cruise. I”. In: *Journal of Aircraft* 6.6 (1969).
- [54] ES Levinsky et al. “Lifting-Surface Theory for V/STOL Aircraft in Transition and Cruise. II”. In: *Journal of Aircraft* 7.1 (1970).
- [55] Rosario MA Marretta. “Performance of a Propeller Embedded in the Flowfield of a Wing”. In: *Journal of Aircraft* 33.5 (1996).
- [56] RM Ardito Marretta et al. “Wing Pitching and Loading with Propeller Interference”. In: *Journal of Aircraft* 36.2 (1999).
- [57] Scott C Rethorst. “Characteristics of an Airfoil Extending Through a Circular Jet”. PhD thesis. California Institute of Technology, 1956.
- [58] Scott Rethorst. “Aerodynamics of Nonuniform Flows as Related to an Airfoil Extending Through a Circular Jet”. In: *Journal of the Aerospace Sciences* 25.1 (1958).
- [59] T Yao-tsu Wu and Richard B Talmadge. *A Lifting Surface Theory for Wings Extending Through Multiple Jets*. Tech. rep. Vehicle Research Corporation, 1961.
- [60] C Ferrari. “Propeller and Wing Interactions at Subsonic Speeds”. In: *Aerodynamic Components of Aircraft at High Speeds*. Ed. by AF Donovan and HC Lawrence. Princeton University Press, 1957.

- [61] G Kleinstein and CH Liu. “Application of Airfoil Theory for Nonuniform Streams to Wing Propeller Interaction”. In: *Journal of Aircraft* 9.2 (1972).
- [62] C. Koning. “Influence of the Propeller on Other Parts of the Airplane Structure”. In: *Aerodynamic Theory*. Springer, Berlin, Heidelberg, 1935.
- [63] M. A. McVeigh, L. Gray, and E. Kisielowski. *Prediction of Span Loading of Straight-wing/Propeller Combinations up to Stall*. Tech. rep. NASA CR-2602. National Aeronautics and Space Administration, 1975.
- [64] Ramadas K. Prabhu. “Studies on the Interference of Wings and Propeller Slipstreams”. PhD thesis. Old Dominion University, 1984.
- [65] Ramadas K Prabhu and Surendra N Tiwari. *Studies on the Interference of Wings and Propeller Slipstreams*. Tech. rep. NASA-CR-175753. National Aeronautics and Space Administration, 1985.
- [66] L. Ting, C. H. Liu, and G. Kleinstein. “Interference of Wing and Multipropellers”. In: *AIAA Journal* (1972).
- [67] Christian Alba et al. “A Surrogate-Based Multi-Disciplinary Design Optimization Framework Exploiting Wing-Propeller Interaction”. In: *18th AIAA/ISSMO Multi-disciplinary Analysis and Optimization Conference*. 2017.
- [68] Julia Ann Cole. “A Higher-Order Free-Wake Method for Aerodynamic Performance Prediction of Propeller-Wing Systems”. PhD thesis. Pennsylvania State University, 2016.
- [69] Julia A Cole et al. “A Practical Application of an Unsteady Formulation of the Kutta-Joukowski Theorem”. In: *35th AIAA Applied Aerodynamics Conference*. AIAA 2017-3904. 2017.
- [70] Ilan Kroo. “Propeller-Wing Integration for Minimum Induced Loss”. In: *Journal of Aircraft* 23.7 (1986), pp. 561–565.
- [71] Michael D Patterson, Matthew J Daskilewicz, and Brian German. “Simplified Aerodynamics Models to Predict the Effects of Upstream Propellers on Wing Lift”. In: *53rd AIAA Aerospace Sciences Meeting*. 2015.
- [72] B Chandrasekaran and G Bartlett. “Method for Calculating Effects of a Propfan on Aircraft Aerodynamics at Subsonic Speeds”. In: *19th Joint Propulsion Conference*. 1983.
- [73] Jinsoo Cho and Marc H Williams. “Propeller-Wing Interaction Using a Frequency Domain Panel Method”. In: *Journal of Aircraft* 27.3 (1990).

- [74] AA Rangwalla and LN Wilson. “Application of a Panel Code to Unsteady Wing-Propeller Interference”. In: *Journal of Aircraft* 24.8 (1987).
- [75] R Hugh Stone. “Aerodynamic Modeling of the Wing-Propeller Interaction for a Tail-Sitter Unmanned Air Vehicle”. In: *Journal of Aircraft* 45.1 (2008).
- [76] Clark B Millikan. “The Influence of Running Propellers on Airplane Characteristics”. In: *Journal of the Aeronautical Sciences* 7.3 (1940).
- [77] R. Smelt and H. Davies. *Estimation of Increase in Lift due to Slipstream*. Tech. rep. R. & M. 1788. Great Britain Aeronautical Research Committee, 1937.
- [78] David Serrano et al. “Effect of disk angle-of-attack on aerodynamic performance of small propellers”. In: *Aerospace Science and Technology* 92 (2019), pp. 901–914.
- [79] Marc L Masquelier. “Application of the Vortex-Lattice Method to Propeller Performance Analysis”. MA thesis. Air Force Institute of Technology, 1982.
- [80] Makoto Kobayakawa and Hiroyuki Onuma. “Propeller Aerodynamic Performance by Vortex-Lattice Method”. In: *Journal of Aircraft* 22.8 (1985), pp. 649–654.
- [81] R Van Houten. *Analysis of Ducted Propellers in Steady Flow*. Tech. rep. AD-A170-384. Naval Sea Systems Command, 1986.
- [82] Daniel J Lesieutre and John P Sullivan. “The Analysis of Counter-Rotating Propeller Systems”. In: *SAE Transactions* 94.4 (1985), pp. 564–575.
- [83] Justin E Kerwin. *The Solution of Propeller Lifting Surface Problems by Vortex Lattice Methods*. Tech. rep. AD-262-648. US Department of the Navy, 1961.
- [84] Anders Smaerup Olsen. “Optimisation of Propellers Using the Vortex-Lattice Method”. PhD thesis. Technical University of Denmark, 2002.
- [85] Hamidreza Abedi, Lars Davidson, and Spyros Voutsinas. “Enhancement of Free Vortex Filament Method for Aerodynamic Loads on Rotor Blades”. In: *Journal of Solar Energy Engineering* 139.3 (2017).
- [86] Juan D Colmenares, Omar D López, and Sergio Preidikman. “Computational Study of a Transverse Rotor Aircraft in Hover Using the Unsteady Vortex Lattice Method”. In: *Mathematical Problems in Engineering* 2015 (2015).
- [87] Joseph Katz and Allen Plotkin. *Low-Speed Aerodynamics*. 2nd Edition. Cambridge University Press, 2001.

- [88] Richard M James. “On the Remarkable Accuracy of the Vortex Lattice Method”. In: *Computer Methods in Applied Mechanics and Engineering* 1.1 (1972), pp. 59–79.
- [89] E Pistolesi. “Considerations Respecting the Mutual Influence of Systems of Airfoils”. In: *Collected Lectures of the 1937 Principal Meeting of the Lilienthal Society*. 1937.
- [90] C Edward Lan. “A Quasi-Vortex-Lattice Method in Thin Wing Theory”. In: *Journal of Aircraft* 11.9 (1974), pp. 518–527.
- [91] Gary R Hough. “Remarks on Vortex-Lattice Methods”. In: *Journal of Aircraft* 10.5 (1973), pp. 314–317.
- [92] Manikandan Ramasamy. “Contributions to the Measurement and Analysis of Helicopter Blade Tip Vortices”. PhD thesis. University of Maryland, 2004.
- [93] S Ananthan, J Gordon Leishman, and M Ramasamy. “The Role of Filament Stretching in the Free-Vortex Modeling of Rotor Wakes”. In: *58th Annual Forum and Technology Display of the Americal Helicopter Society International*. 2002, pp. 11–13.
- [94] Mahendra J Bhagwat and J Gordon Leishman. “Correlation of Helicopter Rotor Tip Vortex Measurements”. In: *AIAA Journal* 38.2 (2000), pp. 301–308.
- [95] Robert JS Simpson, Rafael Palacios, and Joseba Murua. “Induced-Drag Calculations in the Unsteady Vortex Lattice Method”. In: *AIAA Journal* 51.7 (2013), pp. 1775–1779.
- [96] Thomas Lambert and Grigorios Dimitriadis. “Induced Drag Calculations with the Unsteady Vortex Lattice Method for Cambered Wings”. In: *AIAA Journal* 55.2 (2017), pp. 668–672.
- [97] Mark Drela. “Integrated Simulation Model for Preliminary Aerodynamic, Structural, and Control-Law Design of Aircraft”. In: *40th Structures, Structural Dynamics, and Materials Conference and Exhibit*. 99-1394. 1999.
- [98] Nicholas K Borer et al. “Design and Performance of the NASA SCEPTOR Distributed Electric Propulsion Flight Demonstrator”. In: *16th AIAA Aviation Technology, Integration, and Operations Conference*. AIAA 2016-3920. 2016.
- [99] Brandon L Litherland et al. “A Method for Designing Conforming Folding Propellers”. In: *17th AIAA Aviation Technology, Integration, and Operations Conference*. AIAA 2017-3781. 2017.

- [100] Biel Ortun, Ronan Boisard, and Ignacio Gonzalez-Martino. “In-Plane Airloads of a Propeller with Inflow Angle: Prediction vs. Experiment”. In: *30th AIAA Applied Aerodynamics Conference*. AIAA 2012-2778. 2012.
- [101] *OpenVSP*. Accessed: 18 Jun 2020. 2020.
- [102] William M. Chan et al. *Chimera Grid Tools User’s Manual*, v.2.2. 2018.
- [103] Robert Nichols, Robert Tramel, and Pieter Buning. “Solver and Turbulence Model Upgrades to OVERFLOW 2 for Unsteady and High-Speed Applications”. In: *24th AIAA Applied Aerodynamics Conference, Fluid Dynamics and Co-located Conferences*. AIAA 2006-2824. San Francisco, CA, June 2006.
- [104] Robert H. Nichols and Pieter G. Buning. *User’s Manual for OVERFLOW 2.2, v.2.2m*. 2017.
- [105] Andrew K. Henrick, Tariq D. Aslam, and Joseph M. Powers. “Mapped Weighted Essentially Non-Oscillatory Schemes: Achieving Optimal Order Near Critical Points”. In: *Journal of Computational Physics* 207.2 (Aug. 2005), pp. 542–567.
- [106] Robert Tramel, Robert Nichols, and Pieter Buning. “Addition of Improved Shock-Capturing Schemes to OVERFLOW 2.1”. In: *19th AIAA Computational Fluid Dynamics. Fluid Dynamics and Co-located Conferences*. AIAA 2009-3988. American Institute of Aeronautics and Astronautics, June 2009.
- [107] Michael L. Shur et al. “Turbulence Modeling in Rotating and Curved Channels: Assessing the Spalart-Shur Correction”. In: *AIAA Journal* 38.5 (May 2000), pp. 784–792.
- [108] F. R. Menter. “Two-equation Eddy-Viscosity Turbulence Models for Engineering Applications”. In: *AIAA Journal* 32.8 (Aug. 1994), pp. 1598–1605.
- [109] Robin Langtry and Florian Menter. “Transition Modeling for General CFD Applications in Aeronautics”. In: *43rd AIAA Aerospace Sciences Meeting and Exhibit*. Aerospace Sciences Meetings. AIAA 2005-522. American Institute of Aeronautics and Astronautics, Jan. 2005.
- [110] Rohit Jain. “CFD Performance and Turbulence Transition Predictions on an Installed Model-Scale Rotor in Hover”. In: *55th AIAA Aerospace Sciences Meeting*. AIAA 2017-1871. 2017.
- [111] Rohit Jain. “Hover Predictions on the S-76 Rotor with Tip Shape Variation Using Helios”. In: *Journal of Aircraft* 55.1 (2018), pp. 66–77.

- [112] Shishir Pandya and William Chan. “Computation of Sectional Loads from Surface Triangulation and Flow Data”. In: *20th AIAA Computational Fluid Dynamics Conference*. AIAA 2011-3680. 2011.
- [113] Gordon J Leishman. *Principles of Helicopter Aerodynamics*. Cambridge University Press, 2006.
- [114] Richard E Kuhn and William C Hayes Jr. *Wind-tunnel Investigation of Longitudinal Aerodynamic Characteristics of Three Propeller-driven VTOL Configurations in the Transition Speed Range, Including Effects of Ground Proximity*. Tech. rep. NASA-TN-D-55. National Aeronautics and Space Administration, 1960.
- [115] William A Newsom Jr. *Effect of Propeller Location and Flap Deflection on the Aerodynamic Characteristics of a Wing-propeller Combination for Angles of Attack from 0 to 80 degrees*. Tech. rep. NACA-TN-3917. National Advisory Committee for Aeronautics, 1957.
- [116] William A Newsom Jr. *Force-test Investigation of the Stability and Control Characteristics of a Four-propeller Tilt-wing VTOL Model with a Programed Flap*. Tech. rep. NASA-TN-D-1389. National Aeronautics and Space Administration, 1962.
- [117] William A Newsom Jr. *Flight Investigation of the Longitudinal Stability and Control Characteristics of a Four-propeller Tilt-wing VTOL Model with a Programed Flap*. Tech. rep. NASA-TN-D-1390. National Aeronautics and Space Administration, 1962.
- [118] Henry L Kelley, John P Reeder, and Robert A Champine. *Summary of a Flight-test Evaluation of the CL-84 Tilt-wing V/STOL Aircraft*. Tech. rep. NASA-TM-X-1914. National Aeronautics and Space Administration, 1970.
- [119] Robert J Pegg, Henry L Kelley, and John P Reeder. *Flight investigation of the VZ-2 tilt-wing aircraft with full-span flap*. Tech. rep. NASA-TN-D-2680. National Aeronautics and Space Administration, 1965.
- [120] Mark Drela and Harold Youngren. *XROTOR User Guide*. <https://web.mit.edu/drela/Public/web/xrotor/xrotor.doc.txt>. Accessed: 04/30/2021. Nov. 2003.